

Mixing in a Moderately Sheared Salt-Fingering Layer

W. D. SMYTH AND S. KIMURA

College of Oceanic and Atmospheric Sciences, Oregon State University, Corvallis, Oregon

(Manuscript received 25 October 2010, in final form 24 December 2010)

ABSTRACT

Mixing due to sheared salt fingers is studied by means of direct numerical simulations (DNS) of a double-diffusively unstable shear layer. The focus is on the “moderate shear” case, where shear is strong enough to produce Kelvin–Helmholtz (KH) instability but not strong enough to produce the subharmonic pairing instability. This flow supports both KH and salt-sheet instabilities, and the objective is to see how the two mechanisms work together to flux heat, salt, and momentum across the layer.

For observed values of the bulk Richardson number Ri and the density ratio R_ρ , the linear growth rates of KH and salt-sheet instabilities are similar. These mechanisms, as well as their associated secondary instabilities, lead the flow to a fully turbulent state. Depending on the values of Ri and R_ρ , the resulting turbulence may be driven mainly by shear or mainly by salt fingering. Turbulent mixing causes the profiles of temperature, salinity, and velocity to spread; however, in salt-sheet-dominated cases, the net density (or buoyancy) layer thins over time. This could be a factor in the maintenance of the staircase and is also an argument in favor of an eventual role for Holmboe instability.

Fluxes are scaled using both laboratory scalings for a thin layer and an effective diffusivity. Fluxes are generally stronger in salt-sheet-dominated cases. Shear instability disrupts salt-sheet fluxes while adding little flux of its own. Shear therefore reduces mixing, despite providing an additional energy source. The dissipation ratio Γ is near 0.2 for shear-dominated cases but is much larger when salt sheets are dominant, supporting the use of Γ in the diagnosis of observed mixing phenomena. The profiler approximation Γ_z , however, appears to significantly overestimate the true dissipation ratio.

1. Introduction

The interaction of salt fingers with shear is a problem of long-standing interest (e.g., Linden 1974; Kunze 1990, 1994; St. Laurent and Schmitt 1999; Wells et al. 2001; Radko and Stern 2011). Salt-fingering instability is common in the midlatitude thermocline (Stern 1960; Schmitt 2003), where it coexists with shear because of internal wave interactions (e.g., Munk and Wunsch 1998). When fingering instability is especially strong, it forms thermohaline staircases, stacked layers of well mixed fluid separated by interfaces where stratification is strong and fingering is intense (Schmitt et al. 1987). Staircases can drive water-mass transformations that ultimately influence the general circulation (Schmitt et al. 2005). In a staircase, gravity wave shear is focused in the strongly stratified interfaces (Gregg and Sanford 1987). In the presence of lateral gradients, salt fingering can drive

finescale interleaving (Stern 1967; Ruddick and Kerr 2003; Ruddick and Richards 2003). In addition to modulating the ambient internal wave field, interleaving motions generate shear directly in the fingering layers.

In a sequence of theoretical and numerical studies (Smyth and Kimura 2007; Kimura and Smyth 2007; Kimura et al. 2011), we have modeled a sheared fingering layer as a stratified shear layer of hyperbolic tangent form with thermohaline stratification in the salt-fingering regime. Our computations describe instabilities that emerge after the shear has become established.¹ We began with the linear theory for small perturbations (Smyth and Kimura 2007) and established that linear growth rates of fingering and shear-driven instabilities are comparable in much of the oceanic parameter range. Kimura and Smyth (2007) described the first direct numerical simulation (DNS) of this flow geometry. This revealed a sequence of

Corresponding author address: W. D. Smyth, College of Oceanic and Atmospheric Sciences, Oregon State University, Corvallis, OR 97331-5503.
E-mail: smyth@coas.oregonstate.edu

¹ The equally important scenario in which shear is imposed upon preexisting salt fingers (e.g., Kunze 1990; Fernandes and Krishnamurti 2010) is not considered here.

secondary instabilities that led to turbulence with characteristics of both shear forcing and salt fingering.

We now explore beyond the single example described by Kimura and Smyth (2007) by simulating a variety of initial flow states spanning the oceanic parameter regime. In a companion paper (Kimura et al. 2011), we examine what we call the “weak shear” regime, defined by the condition that the minimum Richardson number Ri exceed the critical value $1/4$ (Ri is the nondimensional ratio of squared buoyancy frequency to shear, which is defined explicitly in section 2b). Weak shear causes salt-fingering instability to favor a two-dimensional (2D) planform with rising and sinking sheets of fluid [“salt sheets” (SS)] aligned parallel to the sheared flow (Linden 1974). Shear also modifies the secondary instabilities via which flow becomes turbulent, but it is not strong enough to produce Kelvin–Helmholtz (KH) instability (Miles 1961; Howard 1961). In this regime, the geometry of the primary instability is reflected in the anisotropy of the mixing scales and can therefore seriously affect the interpretation of observational microstructure data. Values for various nondimensional mixing parameters are surprisingly consistent with the predictions of linear theory. Perhaps the most significant result in this regime is that the imposition of a weak shear reduces the rate of mixing.

In the present paper, we address the “moderate shear” regime $0.18 \leq Ri \leq 0.25$. In these flows, shear is strong enough to produce the primary KH instability but is insufficient to produce the subharmonic pairing instability (Collins and Maslowe 1988; Klaassen and Peltier 1989) found at smaller Ri . Although the condition $Ri < 1/4$ is rarely observed directly, it is thought to occur sporadically through random wave interactions (e.g., Muller et al. 1986; Munk and Wunch 1998), and its outcome in the form of KH billows has been clearly identified in the thermocline (e.g., Woods 1968; Kunze et al. 1987).

There are several reasons to suspect that moderate shears, as defined above, are more common than stronger shears ($Ri < 0.18$). First, any shear layer that is accelerated to an unstable state must enter the moderate shear regime first, and the resulting instability acts to retard the acceleration before lower values of Ri are attained. Second, we are unaware of any clear observation of the pairing instability in stratified oceanic flows. Third, the “braids” that separate observed KH billows (Seim and Gregg 1994; Geyer et al. 2010) generally have tilt angles much shallower than the 30° – 45° values that characterize billows in strong shear (e.g., Smyth 2003), suggesting that Ri is not much smaller than $1/4$.

In assessing the competition between salt sheets and shear-driven instability, it is tempting to assume that the former are less important because they are driven by the molecular terms in the equations of motion. However,

the linear, normal mode growth rate of salt sheets does not scale with the molecular diffusivities but rather with the buoyancy frequency. In the “tall finger, viscous control” approximation (e.g., Stern 1975; Kunze 1987; Smyth and Kimura 2007), the growth rate for salt fingers (or, equivalently, for salt sheets) becomes

$$\sigma_{SS} = N f_{SS}(R_\rho), \tag{1}$$

where N is the buoyancy frequency (assumed uniform in this approximation), R_ρ is the density ratio (see section 2b for detailed definitions), and

$$f_{SS}(R_\rho) = \left(\frac{R_\rho}{R_\rho - 1} \right)^{1/2} - 1.$$

The function $f_{SS}(R_\rho)$ is of order unity for common oceanic values of R_ρ and decreases monotonically with increasing R_ρ . In a hypothetical fluid with reduced molecular diffusivities, the salt-sheet wavenumber increases, increasing the gradient that the reduced diffusivities work against and leaving the heat and salt fluxes that drive the instability unchanged. In fact, the growth rates of salt sheets and KH instability are similar over oceanographically common ranges of Ri and R_ρ (Smyth and Kimura 2007). The latter growth rate is given by

$$\sigma_{KH} = S f_{KH}(Ri), \tag{2}$$

where S is the vertical shear of the horizontal current and f_{KH} is a function of Richardson number that decreases monotonically from ~ 0.19 at $Ri = 0$ and becomes 0 for $Ri \geq 0.25$ (Hazel 1972).

This similarity in growth rate does not mean that salt sheets and KH billows are equally important as mixing mechanisms. It could be that nonlinear effects favor one or the other or that one mixes the fluid more efficiently. The present DNS experiments are designed to address those possibilities. As a heuristic first look, consider a simple model of a mixing layer in which the profiles of temperature, salinity, and velocity remain proportional to one another as the layer thickens: that is, the vertical scales over which the three quantities change are all equal to a single length $h(t)$ that increases in time. In that case, the quantities that determine σ_{SS} and σ_{KH} vary with $h(t)$ as follows:

$$N \propto h^{-1/2}; \quad R_\rho \propto h^0; \quad s \propto h^{-1}; \quad Ri \propto h. \tag{3}$$

Substituting (3) into (1), we see that σ_{SS} decreases in proportion to $h^{-1/2}$, so the layer’s ability to support the salt-sheet instability diminishes as h increases. In comparison, (2) shows that σ_{KH} decreases like h^{-1} from its shear dependence alone and more so because of the unspecified decreasing function $f_{KH}(Ri)$. Therefore, the ability of the

thickening interface to sustain KH instability diminishes more rapidly than its ability to support salt sheets. Moreover, in this scenario the upper limit for KH instability, $Ri = 1/4$, is reached in finite time, whereas the corresponding limit for salt sheets, $R_\rho = 1/\tau$ (where τ is the ratio of saline to thermal diffusivity; see section 2b), is never reached. We will see that layer thickening is much more complicated than the picture sketched above. Nonetheless, we will not be surprised to find that, if salt sheets and KH billows start off with similar growth rates, salt sheets will eventually dominate.

In this paper, we use DNS to explore the complex interactions between salt sheets and KH billows and the statistical characteristics of the resulting turbulence. Our methodology is described in section 2. In section 3, we give a brief overview of the sequence of events leading to turbulence. In section 4, we compute diapycnal fluxes and effective diffusivities needed for larger-scale modeling and for interpretation of observational data. In section 5, we explore the evolution of the interface thicknesses and related mean flow parameters. We discuss the dissipation ratio Γ in section 6. In section 7, we investigate the sensitivity of the results to certain parameters whose oceanic values are difficult to reproduce in DNS. Conclusions are given in section 8.

2. Methods

a. The mathematical model

Buoyancy b is defined with respect to the characteristic density ρ_0 and gravitational acceleration g as $b = -g(\rho - \rho_0)/\rho_0$. We assume that the total buoyancy is a simple sum of thermal and saline contributions, $b = b_T + b_S$, each governed by an advection–diffusion equation,

$$\frac{Db_T}{Dt} = k_T \nabla^2 b_T; \quad \frac{Db_S}{Dt} = k_S \nabla^2 b_S. \quad (4)$$

Thermal and saline diffusivities are uniform and are given by κ_T and κ_S , respectively, and, $D/Dt = \partial/\partial t + \mathbf{u} \cdot \nabla$ is the material derivative. The velocity field $\mathbf{u}(x, y, z, t) = (u, v, w)$ is nondivergent and is measured in a nonrotating, Cartesian coordinate system (x, y, z) . The flow is forced by the gradient of the reduced pressure $\pi = p/\rho_0$ and in the vertical by the net buoyancy b . The Boussinesq approximation is assumed. Velocity is diffused by a Laplacian operator with uniform kinematic viscosity ν . The resulting equations are

$$\nabla \cdot \mathbf{u} = 0; \quad \frac{D\mathbf{u}}{Dt} = -\nabla\pi + b\mathbf{k} + \nu\nabla^2\mathbf{u}. \quad (5)$$

The unit vector \mathbf{k} points opposite to gravity.

Boundary conditions are periodic in the horizontal, $f(x + L_x, y, z, t) = f(x, y + L_y, z, t) = f(x, y, z, t)$. Upper and lower boundaries at $z = \pm L_z/2$ are impermeable ($w = 0$) and flux free ($\partial u/\partial z = \partial v/\partial z = \partial b_T/\partial z = \partial b_S/\partial z = 0$). These are placed far enough from the interfacial layer to exert little influence on the early flow development. Simulations are terminated when the disturbances of interest approach the boundaries.

Initial mean profiles are chosen to represent a stratified shear layer,

$$\frac{B_T(z)}{\Delta B_T} = \frac{B_S(z)}{\Delta B_S} = \frac{U(z)}{\Delta u} = \tanh\left(\frac{z}{h}\right). \quad (6)$$

The layer is centered at $z = 0$ and has thickness $2h$. In discussion of thermohaline staircases, it is common to refer to this layer as a step or an interface, even though its non-zero thickness is now thought to be important (e.g., Gregg and Sanford 1987; Kunze 2003). Here, we adopt the term “interface,” except when its thickness is relevant, in which case we use the term “interfacial layer.” The quantity $\Delta B = \Delta B_T + \Delta B_S$ is the half change in net background buoyancy across the interface. Background shear is quantified in terms of Δu , the half change of background velocity.

This background flow is supplemented by a small perturbation added for computational efficiency. The perturbation has two parts. The first is the sum of the fastest-growing eigenfunctions of the Kelvin–Helmholtz and salt-sheet mode from linear theory (Smyth and Kimura 2007). These are normalized such that the maximum vertical displacement of each is $0.02h$. This value was arrived at after significant trial and error. Amplitudes much smaller than $0.02h$ allow viscosity to alter the mean flow before the instability grows, whereas much larger values generate artifacts from the nonlinear terms resulting in amplitude dependence. The second perturbation is a random velocity field focused in a thin layer surrounding the center of the interface. This is needed to initialize subharmonic secondary instabilities of the salt sheets but is made as small as possible so as not to obscure the interactions of the primary KH and salt-sheet modes. The amplitude chosen was such that the maximum value of any velocity component is $10^{-5}\Delta u$. This random velocity field adjusts to a non-divergent state after the first time step.

The semispectral numerical code used to advance (4) and (5) is a modified version of that described by Winters et al. (2004). Saline buoyancy is resolved with half the grid spacing used to resolve the other fields (Smyth et al. 2005).

b. Parameter values

To minimize the number of input parameters, one could nondimensionalize this problem using h as the

length scale and $h/\Delta u$ as the time scale. Any integrated solution quantity f (e.g., eddy diffusivity) could then be expressed in nondimensional form as

$$f^* = \frac{f}{h^a \Delta u^b} = f^*(\text{Ri}, R_\rho, \mu, \tau, \text{Pr}, L_x/h, L_y/h, L_z/h), \quad (7)$$

where the rational numbers a and b are chosen to give the appropriate dimensions for f and the remaining nondimensional parameters are defined below. The gradient Richardson number is defined as

$$\text{Ri} = \frac{N^2}{S^2}, \quad (8)$$

where the squared buoyancy frequency and the shear magnitude are

$$N^2 = \frac{\partial b}{\partial z}, \quad \text{and} \quad S = \left[\left(\frac{\partial u}{\partial z} \right)^2 + \left(\frac{\partial v}{\partial z} \right)^2 \right]^{1/2}. \quad (9)$$

The bulk (minimum) Richardson number at $t = 0$ is $\Delta B h / \Delta u^2$. This is the parameter whose value must be less than $1/4$ to permit KH instability. The buoyancy ratio R_ρ is defined as

$$R_\rho = -\frac{\partial b_T / \partial z}{\partial b_S / \partial z}. \quad (10)$$

At $t = 0$, it has the uniform value $-\Delta B_T / \Delta B_S$.

The Reynolds number is defined in terms of the initial half-velocity change and the half thickness

$$\text{Re} = \frac{\Delta u h}{\nu}. \quad (11)$$

A conceptually useful alternative to the Reynolds number is the ratio of finger width to interface thickness, which we call the aspect ratio μ . Using the ‘‘tall fingers’’ approximation, the salt-sheet wavelength is $\lambda_S = 2\pi h / (\text{Re}^2 \text{RiPr})^{1/4}$, so that

$$\mu = \frac{\lambda_S}{2h} = \pi \text{Re}^{-1/2} \text{Ri}^{-1/4} \text{Pr}^{-1/4}. \quad (12)$$

The salt–heat diffusivity ratio is $\tau = \kappa_S / \kappa_T$, and the Prandtl number is $\text{Pr} = \nu / \kappa_T$.

We can further reduce the number of variable parameters by choosing the domain lengths in terms of the known geometry of KH and salt-sheet instabilities (e.g., Smyth and Kimura 2007). For the present experiments, L_x is set to $2\pi h / 0.47$, a very close approximation to one

wavelength of the KH instability. The domain height is chosen large enough to have no significant influence on the results; we have found that $L_z = L_x$ is sufficient. The term L_y is usually chosen so as to accommodate four wavelengths of the salt-sheet instability, $L_y = 4\lambda_S$ (sensitivity tests with two and eight wavelengths have convinced us that this value is appropriate).

The quantities Pr and τ are molecular properties of saltwater that vary little over the small-scale mixing events considered here and are therefore taken to be constants. Typical oceanic values are $\text{Pr} = 7$ and $\tau = 0.01$. In the present simulations, we choose $\text{Pr} = 7$ and $\tau = 0.04$. The latter choice is a compromise due to computer hardware limitations. Where appropriate, we attempt to assess the difference that reduction of τ to the realistic value 0.01 would make. The aspect ratio μ is also limited by computational resources. Its value is expected to have little influence when $\mu \ll 1$. Here, we choose $\mu = 0.10$. Again, we will attempt to assess the impact of finite μ on our results.

Our main interest is in the impact of the first two parameters of the argument list on the right-hand side of (7), Ri and R_ρ . The standard necessary condition for KH instability is $\text{Ri} < 0.25$ (Miles 1961; Howard 1961). This condition is rarely observed in the ocean, although KH instability is common (Gregg 1987; Thorpe 1987; Geyer and Smith 1987; Seim and Gregg 1994; De Silva et al. 1996; Smyth et al. 2001). It seems likely that small Ri values are either overestimated because of sampling limitations or are short lived; that is, increased by mixing due to the resulting instability before they can be measured. The condition for salt-fingering instability is considerably more relaxed: $1 < R_\rho < \tau^{-1}$ (e.g., Stern 1975). This condition is satisfied over large volumes of the ocean interior (You 2002), though growth is very slow at high R_ρ .

In the midlatitude thermocline, the density ratio is typically not far from 2.0. Lower values, typically less than 1.7, are needed to form staircases (Schmitt 2003). To span the parameter regimes of interest, we use $R_\rho = 1.6, 2.0, 3.0,$ and 25.0 . The final value was chosen equal to $1/\tau$ to exclude the primary salt-sheet instability. For Ri , we use the values 0.18, 0.25, and 0.50. The latter two values exclude KH instability.

To place these parameter choices in the context of the linear theory for the primary KH and salt-sheet modes, we examine linear growth rate curves for the KH (blue) and salt-sheet (red) modes along two lines on the Ri – R_ρ plane (Fig. 1). In all cases, the growth rate is purely real. Line AD starts at a point where $\text{Ri} = 0.18$, low enough to permit KH instability, but $R_\rho = 25$, which is marginally too high to allow salt sheets. We then reduce R_ρ through a sequence of values ending at 1.6 (point D). The KH growth rate is essentially independent of R_ρ and therefore

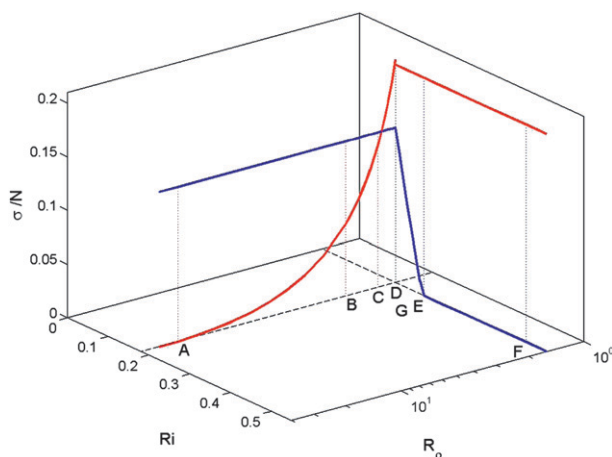


FIG. 1. Growth rate curves for SS (red) and KH (blue) modes normalized by the buoyancy frequency and plotted as functions of Ri and R_p . The Prandtl number, the diffusivity ratio, and the aspect ratio are fixed at $Pr = 7$, $\tau = 0.04$, and $\mu = 0.1$, respectively. The methodology is described in Smyth and Kimura (2007). Vertical dotted lines indicate values used for DNS.

does not vary, but the SS growth rate increases monotonically. At the second-to-last value, $R_p = 2$ at point C, the growth rates of the two modes are equal, and at point D the salt-sheet mode grows faster. Along line \overline{DF} , R_p is held constant at 1.6 while Ri is increased. The change in Ri has no effect on the salt-sheet growth rate, but it causes the KH growth rate to drop to zero near $Ri = 0.25$ and to remain there. We therefore expect that only salt sheets will grow in cases E and F.

In what follows, we will not present our results in the nondimensional form (7). Instead, to facilitate comparison with observations, we use a dimensional form based on assuming a known value for the buoyancy frequency N . The dimensional length and velocity scales are then

$$h = \left(\frac{\nu}{N}\right)^{1/2} \frac{\pi}{Pr^{1/4}\mu}; \quad \Delta u = \frac{(\nu N)^{1/2}}{Pr^{1/4}Ri^{1/2}} \frac{\pi}{\mu}. \quad (13)$$

We set N equal to 0.015 s^{-1} , a typical value for interfaces in a thermohaline staircase (Kunze 2003). For the cases we consider most thoroughly here, $h = 0.16 \text{ m}$ and $\Delta u = 5.8 \times 10^{-3} \text{ m s}^{-1}$. The initial layer thickness is smaller than usual for observed staircases, though it soon increases (section 5). In the Caribbean-Sheets and Layers Transect (C-SALT) staircase, interface thickness was estimated visually from profiles as 2–5 m (Gregg and Sanford 1987). If the thickness of a hyperbolic tangent function were to be estimated in the same way, one might obtain at most $4h$, or 0.6 m. We therefore have the classic problem of DNS: to resolve the smallest scales

TABLE 1. Parameter values for all cases. In every case $Pr = 7$. Here, $L_y = 4\lambda_S$, except for in cases Ct04 and Ct01, where $L_y = 2\lambda_S$.

Label	Ri	R_p	μ	τ	Fine grid size
A	0.18	25.0	0.10	0.04	$512 \times 64 \times 1024$
B	0.18	3.0	0.10	0.04	$512 \times 64 \times 1024$
C	0.18	2.0	0.10	0.04	$512 \times 64 \times 1024$
D	0.18	1.6	0.10	0.04	$512 \times 64 \times 1024$
E	0.25	1.6	0.10	0.04	$512 \times 64 \times 1024$
F	0.50	1.6	0.10	0.04	$512 \times 64 \times 1024$
Cm13	0.18	2.0	0.13	0.04	$512 \times 80 \times 1024$
Cm06	0.18	2.0	0.064	0.04	$768 \times 64 \times 1536$
Ct04	0.18	2.0	0.10	0.04	$512 \times 32 \times 1024$
Ct01	0.18	2.0	0.10	0.01	$1024 \times 64 \times 2048$

with finite memory, we must artificially reduce the largest. As a result, all conclusions are subject to revision as larger computers become available. Parameter values for 10 cases analyzed here are given in Table 1.

3. Overview of flow evolution

Turbulence develops via a sequence of primary (Fig. 1) and secondary instabilities. In the case of equal growth rates (case C), both KH and SS instabilities are clearly visible early in the flow evolution (Fig. 2a). Also visible on the upper extremities of the salt sheets is a propagating secondary instability excited by the interaction of salt sheets and KH billows. To understand this instability, first imagine the salt sheets “slicing” the billows by advecting them alternately up and down at different cross-stream locations, as is illustrated in Fig. 2a. If the salt sheets were infinitely tall, this simple picture would be accurate. In the present case, however, the salt sheets have tips beyond which their influence decreases sharply. Buoyant fluid within each sheet is compressed against the ambient fluid, amplifying vertical gradients in temperature, salinity, and horizontal velocity. The net result of these gradients is to increase shear and reduce net stratification (i.e., reduce the Richardson number), as shown in Fig. 3. Therefore, as a salt sheet grows, the region within it where $S^2 > 4N^2$, or $Ri < 1/4$, is displaced vertically away from the center of the interfacial layer and into regions where the background current is nonzero (arrows in Fig. 3). This promotes the growth of unstable modes with nonzero phase velocity: rightward (leftward) in upgoing (downgoing) salt sheets. The preference for propagating instabilities increases as the salt sheets grow, both because the gradients at the tips become stronger and because the unstable regions are displaced farther from the center of the interfacial layer where the horizontal velocity is greater. Because of its localized shape, the propagating mode excites motions on a range of length scales on the outer edges of the interfacial layer (Fig. 2b).

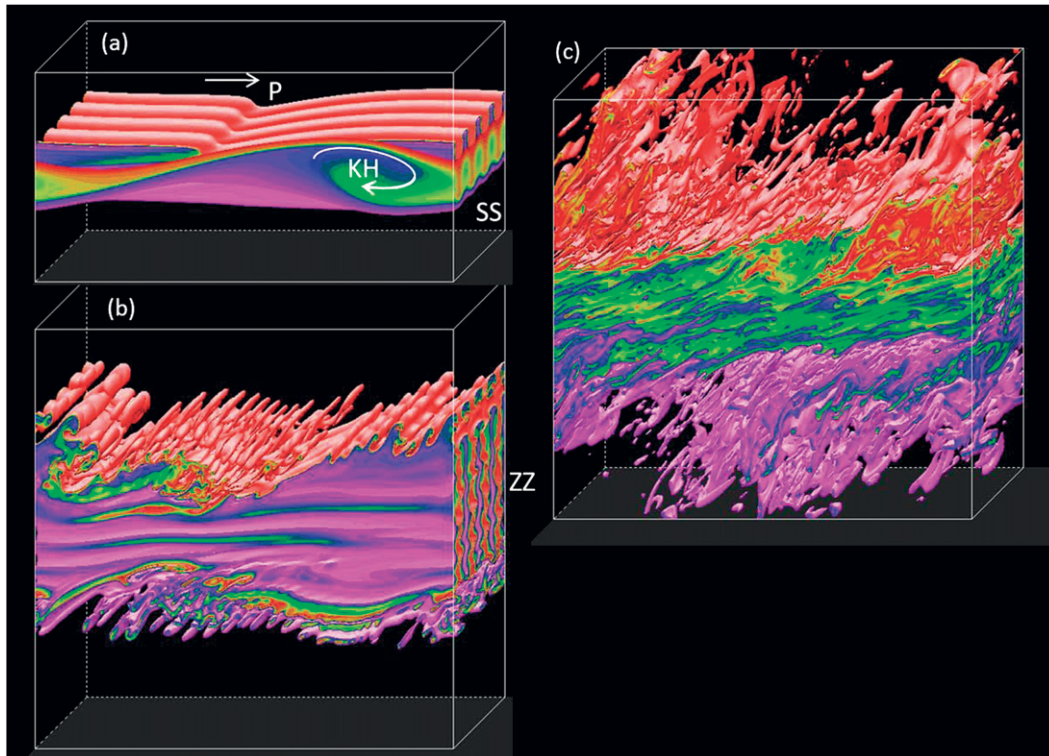


FIG. 2. Saline buoyancy field for case C ($Ri = 0.18$ and $R_p = 2$) at (a) $t = 2000$ s, (b) $t = 3500$ s, and (c) $t = 4500$ s. Annotations indicate the KH billow, the SS, the upper propagating instability (denoted as P), and the ZZ instability. The vertical range $-3/8L_z < z < 3/8L_z$ is shown in (c). The vertical range is smaller in (a) and (b). Colors range from $-0.6\Delta B_S$ (purple) to $0.6\Delta B_S$ (red); values outside this range are rendered transparent.

Within the interfacial layer, salt sheets manifest the zigzag (ZZ) mode of secondary instability (e.g., Holyer 1984; Stern and Simeonov 2005; see Fig. 2b). Previous studies of this instability have focused on the two-dimensional case. Here, the background shear renders the primary instability two dimensional so that the similarity with the earlier results is clear.

Seen in Fig. 2b is a three-dimensional extension of the zigzag mode having a broadband structure in the streamwise direction that is manifested in quasi-horizontal streaks visible on the front face of the figure. These streaks have been suggested as the origin of the near-horizontal laminae seen in shadowgraph images from the C-SALT experiment (Kunze et al. 1987; Kimura and Smyth 2010, manuscript submitted to *J. Mar. Res.*).

This combination of primary and secondary instabilities leads the flow to a fully turbulent state (Fig. 2c). In the interfacial layer, anisotropy due to the background shear is evident, whereas in the outer layer the turbulence consists mainly of convective plumes. In cases dominated by KH instability, transition occurs via the Klaassen–Peltier (KP) secondary instability (Klaassen and Peltier 1991).

4. Fluxes and diffusivities

The vertical fluxes through the interface are of primary importance in understanding the impact of salt fingers and KH billows on the larger-scale flow. Here, we define the fluxes of saline, thermal, and net buoyancy and horizontal velocity as

$$\begin{aligned} F_{bs}(z, t) &= \overline{w'b'_S}, & F_{bT}(z, t) &= \overline{w'b'_T}, \\ F_b(z, t) &= \overline{w'b'}, & F_u(z, t) &= \overline{w'u'}, \end{aligned} \quad (14)$$

where the overbar denotes the horizontal average and the primes deviations from it.

We begin the discussion by focusing on case C, where R_p and Ri are such that the growth rates of the primary salt-sheet and KH instabilities are equal (section 4a). Note that, for different values of various secondary parameters (e.g., τ , μ , initial noise amplitude), the curve on the R_p – Ri plane where these growth rates are equal is likely to shift (see section 7 for a fuller discussion). However, conclusions about the results of moving away from this curve in one way or another are likely to remain valid. Following the case of equal growth rates, we explore several cases in

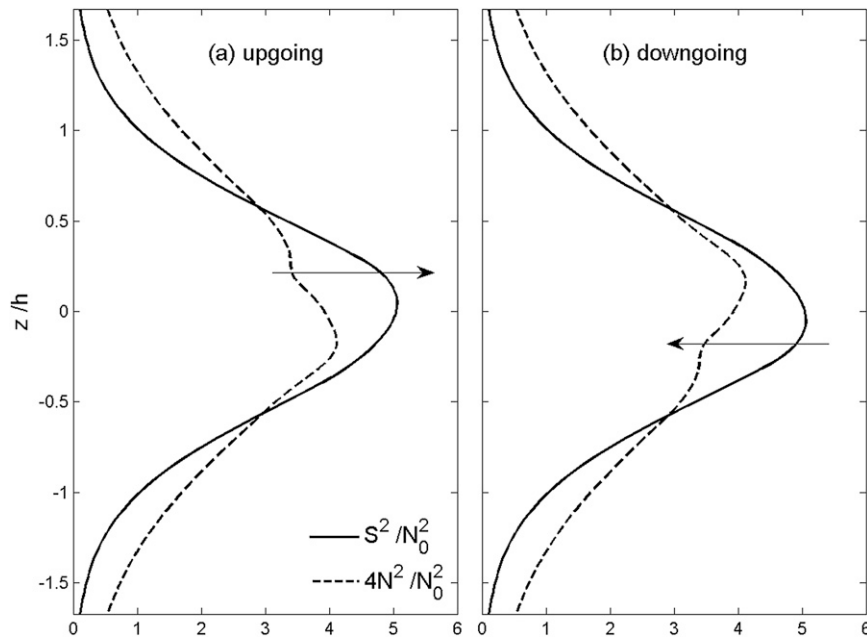


FIG. 3. Mean profiles of the squared shear S^2 and 4 times the stratification N^2 , averaged over x at spanwise locations corresponding to (a) upgoing and (b) downgoing SS. Here, N^2 is multiplied by 4 because $S^2 > 4N^2$ implies $Ri < 1/4$. Arrows indicate background flow direction at the heights where $S^2 - 4N^2$ is largest. For case C and $t = 600$ s.

which growth rates are made unequal, first by varying R_ρ to control the strength of salt-sheet instability and by varying Ri to alter the KH billows (section 4b).

a. The case of equal growth rates

KH instability results in a downward buoyancy flux $F_b < 0$, whereas salt sheets drive an upward buoyancy flux $F_b > 0$. In case C, the buoyancy flux is dominated by salt sheets (Fig. 4), except for a brief initial interval ending at $t = 1500$ s during which downward flux due to KH is evident (see arrow). After this, salt-sheet-driven positive flux grows and spreads steadily until $t = 3300$ s, beyond which the flux evolution changes dramatically. Within the interfacial layer, oscillations emerge with period ~ 200 s. At the same time, the vertical extent of the flux begins to grow much more rapidly. This transition corresponds to the emergence of the propagating secondary instability described in section 3. Figure 2 shows both the wavelike features at the edges of the interfacial layer responsible for the periodic flux reversals and the plumes that carry the buoyancy flux outward. The wavelike oscillations in the interfacial layer destroy the coherent salt sheets (Fig. 2a) that had previously carried the strong buoyancy flux, and the central buoyancy flux drops to near 0. Around $t = 5000$ s, the flux reaches the domain boundaries, and buoyant fluid begins to pool there. This effect propagates inward, progressively neutralizing the flux and signaling the end of the useful period of the simulation.

In the context of a thermohaline staircase, heat and salt fluxes across the interface are important both because they determine the net flux through the staircase and because they set the structure of the staircase. The saline buoyancy flux (Fig. 5, dashed) is generally positive. It grows exponentially in the linear regime, drops slightly as the KH billows are destroyed at $t = 1800$ s, and then grows more rapidly with the onset of secondary instability. The destruction of the salt sheets around $t = 4000$ s causes F_{bS} to drop to near-0 values. The large values attained during the development of turbulence compare well with the $\Delta B_S^{4/3}$ law obtained by Kelley (1986) from the laboratory results of Schmitt (1979a) and McDougall and Taylor (1984) and conveniently summarized in Hebert (1988),

$$F_{b\text{Slab}} = C(R_\rho) k_T^{1/3} \Delta B_S^{4/3},$$

with

$$C(R_\rho) = 0.04 + 0.374 R_\rho^{-1.19}. \quad (15)$$

The thermal buoyancy flux (dashed-dotted curve in Fig. 5) evolves similarly to the saline flux except for the expected sign difference. The net buoyancy flux (solid), as seen above, starts off negative because of the initial dominance of KH instability but reverses sign as salt sheets attain large amplitude. Shown for comparison is an order of magnitude estimate based on setting the Stern number $F_b/\nu N^2$ to unity (Stern 1969). The estimates of F_{bS} and F_b both work

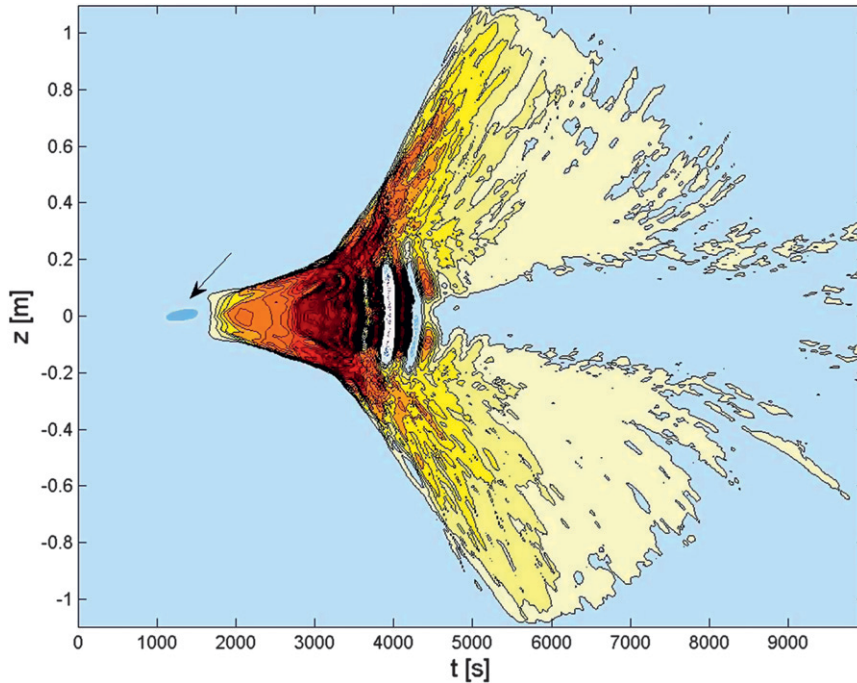


FIG. 4. Horizontally averaged buoyancy flux at $z = 0$ for case C. Black (white) contours with red (blue) shading indicate positive (negative) fluxes. Light blue shading indicates 0 flux. The contour interval is $7.15 \times 10^{-11} \text{ W kg}^{-1}$. Arrow indicates negative flux due to KH billow.

reasonably well in the turbulent phase, though a higher Stern number (e.g., $F_b/\nu N^2 = 2$) would give a better fit.

The ratio of (minus) thermal to saline buoyancy fluxes is the flux ratio γ . In the linear theory of small-amplitude salt sheets, this parameter is a simple function of R_ρ (e.g., Stern 1960, 1975; Schmitt 1979b; Kunze 1987, 2003) and is generally close to 0.6. In contrast, if one assumes that the saline and thermal diffusivities are equal, as is approximately true for shear-driven turbulence, then $\gamma = R_\rho$. This is very nearly true for KH billows, because salt and heat are advected together. In our case C, early values of γ are between 0.6 and R_ρ (Fig. 6, thin curve), suggesting a combination of KH and salt-sheet influences. During the development of turbulence in the interfacial layer, γ first oscillates and then converges to something very near the linear value for salt sheets. A more stable estimate is obtained by averaging the fluxes over the entire computational volume before taking the ratio (Fig. 6, thick curve). This remarkable agreement between linear theory and fully turbulent flow was also noted by Kimura and Smyth (2007).

Assuming that the centerline fluxes are driven by the local gradients, we can attempt to represent them via a diffusivity,

$$F_{bS} = -K_S(t) \frac{\partial \overline{b_S}}{\partial z}, \quad (16)$$

where the gradient is evaluated at the centerline (and similarly for the thermal buoyancy, net buoyancy, and momentum fluxes). Results are shown in Fig. 7. In the linear regime ($0 \text{ s} \leq t \leq 1500 \text{ s}$), all effective diffusivities are positive and grow exponentially as expected. Near

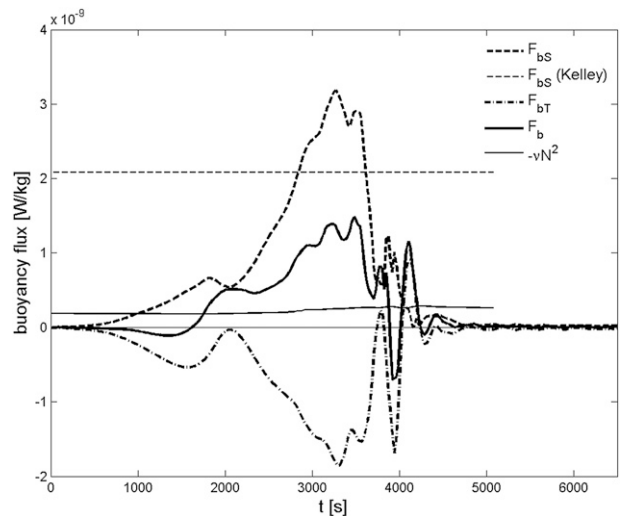


FIG. 5. Horizontally averaged buoyancy flux components at the centerline, $z = 0$, for case C. The thin dashed line shows the parameterization (15) for F_{bS} . The thin solid curve shows the net buoyancy flux estimated from the Stern (1969) criterion, $F_b/\nu N^2 = 1$.

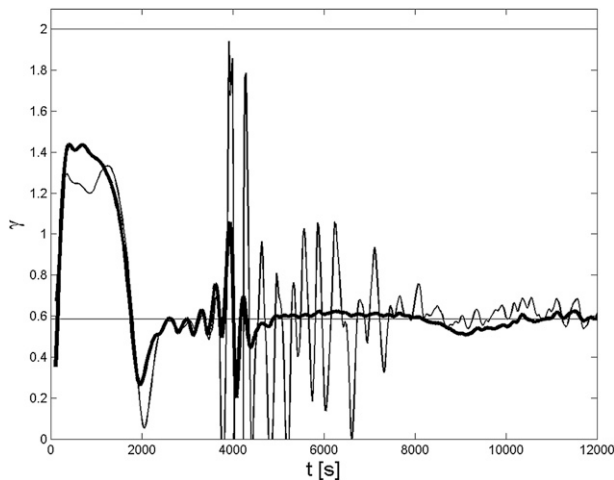


FIG. 6. Flux ratio for case C based on volume-averaged fluxes (thick curve) and on fluxes at the centerline (thin curve). Horizontal lines indicate $\gamma = R_\rho$, the value for shear-driven turbulence, and $\gamma = 0.59$, the value for the fastest-growing linear SS mode.

$t = 1600$ s, growth is temporarily reversed and K_ρ changes sign as salt sheets become dominant. Growth resumes around $t = 2000$ s and continues until the salt sheets are destroyed. The saline diffusivity (dashed curve) peaks at $4 \times 10^{-5} \text{ m}^2 \text{ s}^{-1}$, which is 4 times the canonical value $10^{-5} \text{ m}^2 \text{ s}^{-1}$ for thermocline mixing (Gregg 1998). This condition is brief, though, lasting only as long as salt sheets remain coherent. As secondary instability destroys the salt sheets, the diffusivity drops to near zero (just as the centerline fluxes do in Fig. 5). The thermal diffusivity (dashed-dotted) is considerably smaller than the saline diffusivity, as expected for salt sheets. The effective mass diffusivity (solid) is of similar magnitude but opposite sign, reflecting the tendency of salt sheets to create fluid of anomalous density that can then propagate large distances in the vertical, leaving behind amplified density stratification. The momentum diffusivity (dotted) is positive but extremely small, rarely even exceeding the molecular viscosity.

The centerline diffusivities discussed above give an incomplete picture, especially later in the simulation when strong fluxes driven by salt fingering move away from the centerline (Fig. 4). These fluxes are nonlocal in nature; that is, they are independent of the local gradient. Nonetheless, we can form a diffusivity describing the whole volume by integrating (16) in the vertical and solving for K_S . This results in

$$K_S^{\text{vol}}(t) = -\frac{\int_{-L_z/2}^{L_z/2} F_{bs} dz}{\int_{-L_z/2}^{L_z/2} (\partial b_S / \partial z) dz} \approx -\frac{\int_{-L_z/2}^{L_z/2} F_{bs} dz}{\Delta B_S}. \quad (17)$$

The second equality is valid until altered fluid contacts the boundaries. This approximation suggests that the

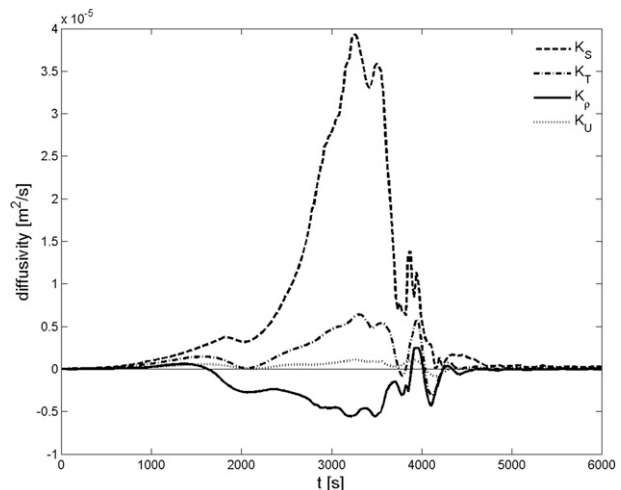


FIG. 7. Evolution of the effective saline, thermal, mass, and momentum diffusivities for case C, evaluated at the centerline ($z = 0$) from horizontally averaged fluxes and gradients [e.g., (16)].

integrated flux away from the layer depends on the property change across the layer, even though the flux and the gradient are not spatially collocated. The resulting diffusivities (Fig. 8) are similar to those found at the centerline (Fig. 7), except that their maxima are smaller and they remain nonzero at late times, reflecting the propagation of salt fingers away from the interface. Oscillations near the diffusivity peak $t \approx 3500$ s reflect the propagating secondary instability (section 3). These are not evident in the centerline diffusivities (Fig. 7) as the propagating mode is focused away from the centerline.

As is evident in Figs. 7 and 8, the momentum diffusivity is very small in this simulation. This is generally true for salt sheets, as was predicted by Ruddick et al. (1989) and verified in the DNS of Kimura and Smyth (2007). The Schmidt number $Sc = K_U/K_S$ should be of order unity for KH billows but is predicted to be much smaller for salt sheets on the basis of linear theory (Smyth and Kimura 2007). Early in the simulation, Sc lies between the salt-sheet and KH regimes (Fig. 9), reflecting the dual influence of those processes. For $t > 7000$ s, the centerline Schmidt number (thin curve) oscillates around the value predicted from linear theory (Smyth and Kimura 2007). The value based on volume averages (thick curve) oscillates around zero, even becoming negative at times. This reflects the presence of off-axis fluxes that are not governed by the initial shear. These are most likely driven by the convective action of salt sheets far from the transition zone.

b. The influence of R_ρ and Ri

Figure 10 shows the buoyancy flux evolution for case B, where R_ρ was increased to 3. The linear growth rate of the salt sheets is now significantly smaller than that of

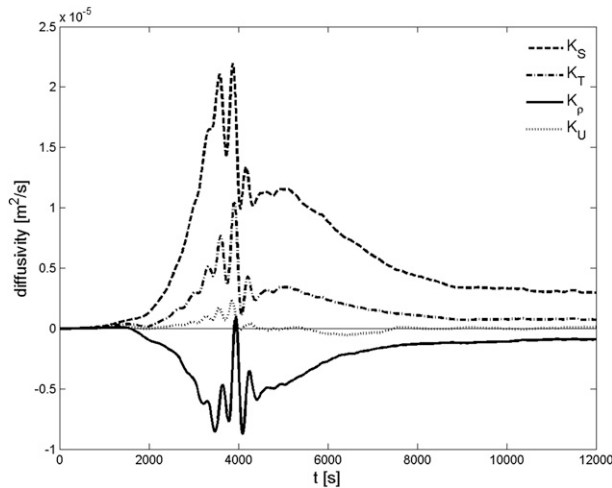


FIG. 8. Evolution of the effective saline, thermal, mass and momentum diffusivities for case C, evaluated from volume-averaged fluxes and gradients as in (17).

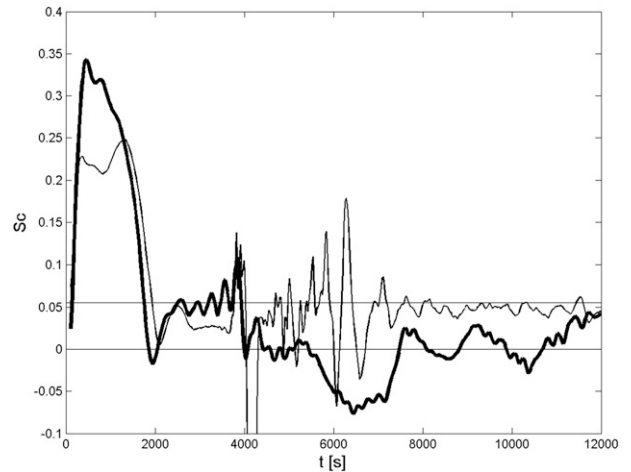


FIG. 9. Schmidt number for case C, based on volume averages (thick curve) and on fluxes and gradients at the centerline (thin curve). Horizontal lines indicate 0 and $Sc = 0.06$, the value for the fastest-growing linear mode.

the KH instability. The negative buoyancy flux characteristic of KH instability is dominant until about 4500 s. Beyond that point, the flux becomes oscillatory because of both the nutation of the billow and the KP secondary instability (Klaassen and Peltier 1991), which is convective in origin and hence drives an upward buoyancy flux. The buoyancy flux due to the salt fingers seen in Fig. 10 is much smaller than that due to the KH billows and is thus barely visible with this contour interval.

We next compare the evolution of the saline buoyancy flux across the interface for cases B, C, and D, in which $Ri = 0.18$ and R_ρ is set at 3 (with weak salt sheets), 2, and 1.6 (with salt sheets dominant). Fluxes at $z = 0$ are shown in Fig. 11a. Figure 11b shows versions scaled by the laboratory-based law (15) and by the approximate growth rate (1). In each case, the flux grows to a maximum and then decays. Both amplitude and timing of the peak in flux are collapsed well by these scalings. (The pure KH case, case A, is omitted because it does not scale well, as expected.) In the first case ($R_\rho = 3$, dashed-dotted), the saline buoyancy flux is relatively small. Oscillations evident in Fig. 11b correspond to the nutation of the KH billow (e.g., Klaassen and Peltier 1985). The flux is largest in the third case ($R_\rho = 1.6$, solid), with dramatic reversals around $2000\text{ s} < t < 3000\text{ s}$ because of the propagating secondary instability.

Comparing the evolution of the effective saline diffusivity in the same three cases (Fig. 12), we see that K_S is generally smaller at higher R_ρ . Because the mixing event is both transient and spatially nonlocal, we do not attempt to capture the diffusivity in a single number but instead show how a maximally simple scaling can collapse the

curves for the various cases. An exponential dependence on R_ρ has been used previously in modeling studies (Walsh and Ruddick 1998; Mueller et al. 2007; Smyth and Ruddick 2010). Here, we use this dependence with constants determined via a visual fit,

$$K_{Sscale} = 1.0 \times 10^{-4} \text{ m}^2 \text{ s}^{-1} R_\rho^{-2.5}. \quad (18)$$

The dependence $R_\rho^{-2.1}$ used by Smyth and Ruddick (2010) and based on the 2D simulations of Stern et al. (2001) collapses the curves nearly as well.

From the examples with $Ri = 0.18$ discussed above, we have seen that both fluxes and diffusivities are greatest when salt sheets are the dominant mixing mechanism and decrease as salt sheets are damped by increasing R_ρ . We turn next to the dependence of the centerline saline diffusivity on Ri (Fig. 13). We begin with case D ($R_\rho = 1.6$ and $Ri = 0.18$), the case with the largest diffusivity of the previous sequence, and increase Ri to 0.25 (case E, dashed) and 0.50 (case F, dashed-dotted). KH instability is present in the first case, not in the latter two. The oscillations due to the propagating secondary instability are damped in the higher Ri cases, as we would expect because of the reduced shear. Except for a brief peak, K_S is greatest in the cases with elevated Ri .

We have seen similar results for a sequence with $R_\rho = 2$ (not shown). Evidently, in this moderate shear regime, shear disrupts the mixing mechanisms associated with salt-sheet instability while contributing very little mixing of its own, even via KH instability. In other words, despite providing an additional energy source, increased shear actually reduces mixing. Kimura et al. (2011) find a similar

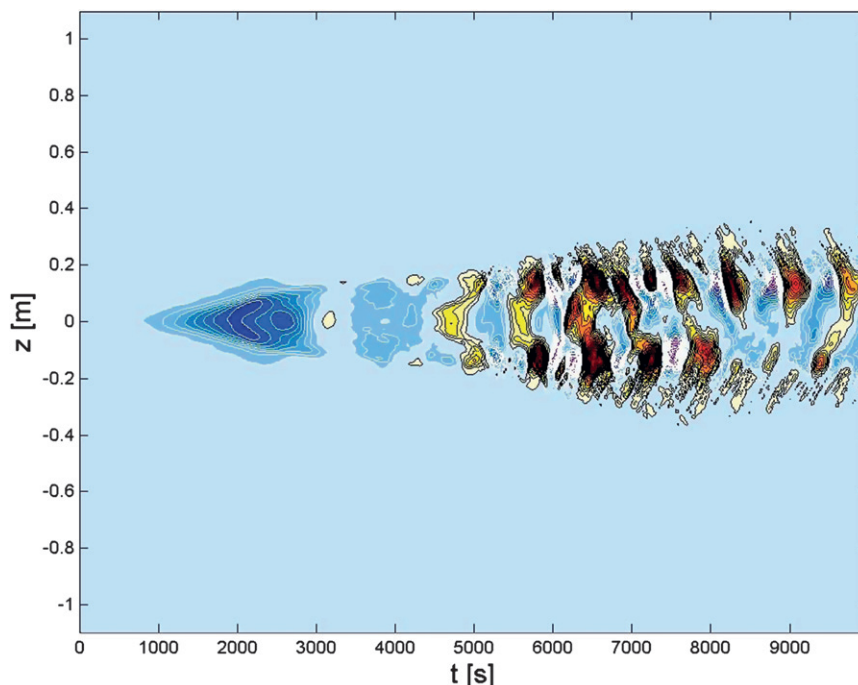


FIG. 10. Horizontally averaged buoyancy flux at $z = 0$ for case B, for comparison with Fig. 4. Black (white) contours indicate positive (negative) fluxes. The contour interval is $5.19 \times 10^{-11} \text{ W kg}^{-1}$.

result for Ri ranging from 0.5 to ∞ , even though KH instability is not present in those cases.

Model parameterizations of small-scale mixing are usually based on an assumption of stationary turbulence, so that mixing rates have no explicit dependence on time. If that condition is valid, one can predict the fluxes conveniently using a single value of the diffusivity. In the present case, the transience of the mixing invalidates this approach.² A more appropriate choice is to parameterize some measure of the net mixing by the entire event: for example, the time-integrated buoyancy flux across the interfacial layer. One is then left with the problem of determining the frequency of such events, but that is beyond our scope here. The collapse of the saline buoyancy flux evolution by (1) and (15) shown in Fig. 11 suggests a parameterization for the time-integrated flux that may have some generality,

$$\int_0^{\infty} F_{\text{bs}} dt = A \frac{C(R_\rho) k_T^{1/3} \Delta B_S^{4/3}}{N f_{\text{SS}}(R_\rho)}, \quad (19)$$

where the constant A is the area under any of the curves shown in Fig. 11b. Values of A for cases B–D ($Ri = 0.18$ and $R_\rho = 3.0, 2.0,$ and 1.6) are 9.5, 12.0, and 9.5,

² In the weak shear regime (Kimura et al. 2011), smaller values of μ are accessible; as a result, the turbulent regime is quasi-stationary, allowing meaningful calculation of an effective diffusivity.

respectively, suggesting that (19) with $A = 10$ predicts the time-integrated flux to within 30% for $Ri = 0.18$. We can do the same for the three cases in which Ri was varied (Fig. 13). There, the collapse is trivial because the parameters involved in (1) and (15) do not change. We find that, for cases D–F ($R_\rho = 1.6$ and $Ri = 0.18, 0.25,$ and 0.50), $A = 9.5, 9.9,$ and 10.6 , respectively. The change in A can only result from the difference in Ri among these cases, and it therefore provides a quantitative measure of the effect of background shear. A least squares fit gives $A = 11.34 Ri^{0.097}$. Our representative value of 10 for A remains within 30% over this range of Ri . The exponent 0.097 is comparable to the value 0.17 obtained for the weak shear regime (Kimura et al. 2011).

In early laboratory experiments on sheared salt fingers, Linden (1974) found a tendency opposite to that seen here—finger fluxes increased with increasing shear—but attributed it to limitations of the apparatus and suggested that there is actually no dependence. The weak Ri dependence found here is not far from Linden’s prediction. More recently, Fernandes and Krishnamurti (2010) found dependences equivalent to $Ri^{0.0125}$, $Ri^{0.05}$, and $Ri^{0.17}$ for $R_\rho = 1.2, 1.54,$ and 2.1 , respectively. (These are converted from their Reynolds number dependence using the fact that, because all factors other than flow velocity are constant, $Re \sim Ri^{-1/2}$.) The exponents agree with ours in both sign and approximate magnitude. This is despite differences

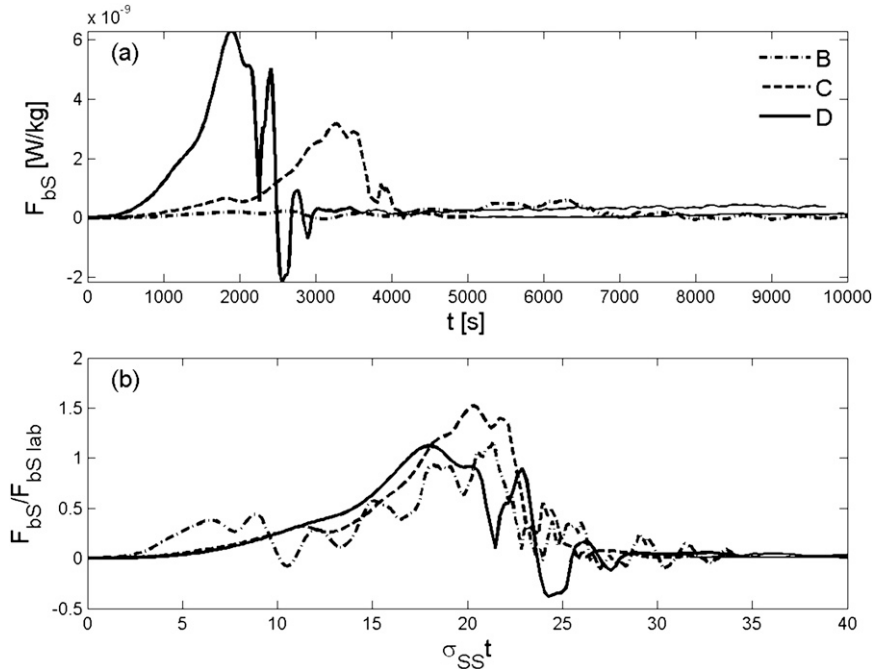


FIG. 11. (a) Evolution of the saline buoyancy flux at $z = 0$ for three cases with $Ri = 0.18$ and $R_p = 3.0$ (case B), 2.0 (case C), and 1.6 (case D). (b) Fluxes are scaled by the thin interface law (15), and times are scaled by the growth rate (1).

in fluid properties (Fernandes and Krishnamurti used sugar and salt as solutes) and initial conditions (salt fingers were already established when the shear was turned on).

5. Evolution of the layer thickness, bulk Richardson number, scale ratio, and density ratio

One manifestation of the fluxes discussed above is in the thickening of the interfacial layer. As noted in the introduction, if the mean profiles thicken such that the length scales of U , B_S , and B_T remain equal, some aspects of the competition between KH instability and salt sheets are easily predicted. We will now see how that thickening actually proceeds.

The integral scale is a useful measure of thickness for interfacial profiles. The integral scale for the horizontally averaged velocity, for example, is defined by

$$I_U = \int_{-L_z/2}^{L_z/2} \left[1 - \left(\frac{\bar{u}}{\Delta u} \right)^2 \right] dz. \tag{20}$$

If \bar{u} is a hyperbolic tangent profile of the form (6), $I_U = 2h$ as long as $h \ll L_z$. By construction, integral scales for all profiles start out equal to $2h$ (Fig. 14). The velocity scale increases at a nearly constant rate. The salinity and temperature scales increase slowly in the linear regime, then rapidly as the propagating secondary instability grows,

and then slowly again as the flow becomes fully turbulent. The thickness of the net buoyancy profile decreases by about 60% and then remains approximately steady. The vertical line indicates the time of contact with the upper and lower boundaries. Beyond this time, the integral scale must be interpreted with caution as the profiles depart significantly from the hyperbolic tangent form. In this case, though, no particular change in behavior is evident, suggesting that the integral scale remains a useful measure of layer thickness.

We now move beyond the case $R_p = 2$ (case C) and look at the dependence of the integral scale for buoyancy on R_p . Figure 15a shows the evolution of I_b for four cases over which R_p varies from 1.6 (solid) to 25 (dotted). The dotted and dashed-dotted curves ($R_p = 25$ and 3, respectively) represent cases where double diffusion is weak or non-existent. In these cases, the buoyancy interface thickens as expected in shear-driven mixing. In contrast, salt sheets are dominant in the cases $R_p = 2$ (dashed curve; cf. solid in Fig. 14) and $R_p = 1.6$ (solid), and the buoyancy interface thins.

The evolution of the interfacial layer thicknesses as shown in Figs. 14 and 15a implies changes in the associated bulk values of the three parameters that control shear and double-diffusive instability: the Richardson number, the velocity–density scale ratio, and the density ratio. These evolve as

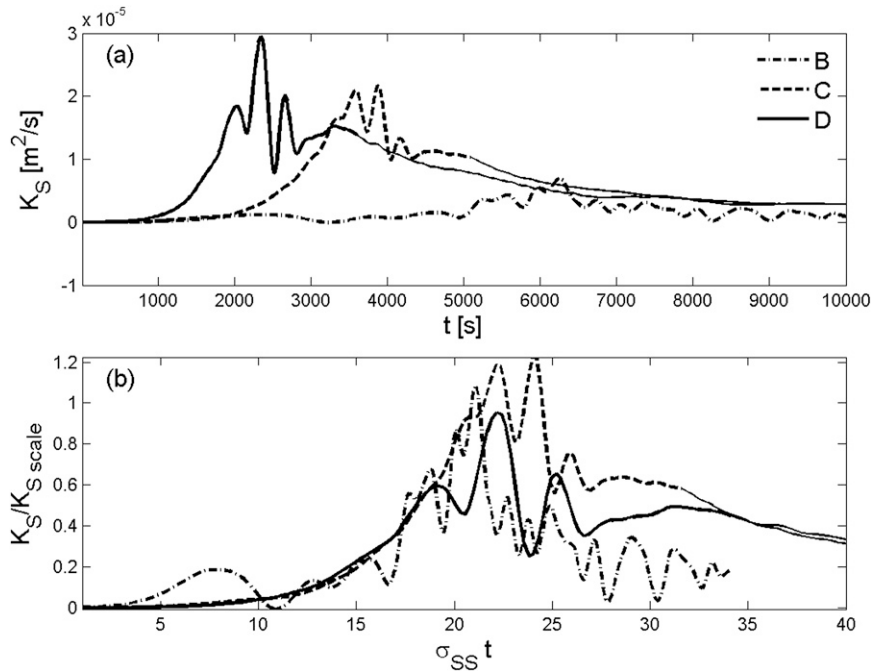


FIG. 12. (a) Evolution of the effective saline diffusivity based on (17) for three cases with $Ri = 0.18$ and $R_\rho = 3.0$ (case B), 2.0 (case C), and 1.6 (case D). (b) Diffusivities are scaled by the empirical fit (18), and times are scaled by the growth rate (1).

$$\begin{aligned}
 Ri(t) &= \frac{\Delta B}{\Delta u^2} \frac{I_u(t)^2}{2I_b(t)}, & R(t) &= \frac{I_u(t)}{I_b(t)}, & \text{and} \\
 R_\rho(t) &= -\frac{\Delta B_T}{\Delta B_S} \frac{I_{bS}(t)}{I_{bT}(t)}, & & & (21)
 \end{aligned}$$

respectively. The central Richardson number increases in all cases, but especially fast in the cases dominated by salt sheets (where the increase is due both to shear layer thickening and stratified layer thinning). In all cases, $Ri(t)$ eventually exceeds 0.32, the approximate value where turbulence due to shear instability begins to decay (Thorpe 1971; Smyth and Moum 2000b). The quick and dramatic passing of this value in the low R_ρ cases no doubt accounts for the rapid quenching of KH instability. When the scale ratio R exceeds 2 (Fig. 15c), KH instability may be supplanted by Holmboe instability, even if Ri is large (Alexakis 2005). The growth of R in the double-diffusive cases suggests that Holmboe instability could play a role in the late evolution of the interfacial layer. A hint of this is evident on close inspection of Fig. 2. Although the Holmboe instability criterion $R > 2$ for parallel, hyperbolic tangent flow profiles is only marginally satisfied at that stage, deviations from the standard form can alter that criterion. We have seen an example in the growth of the propagating secondary instability (section 3).

In the introduction, we noted that, if salinity and temperature mixed such that I_{bS} and I_{bT} remained equal, R_ρ

would remain constant. Figure 15d shows that this is not quite true. In the cases where R_ρ is small enough to allow salt-sheet instability, it grows over time, from 1.6 to 2.3, from 2.0 to 3.0, and from 3.0 to 3.7. These changes make the interface somewhat less susceptible to salt sheets. In the case shown by the dotted curve, R_ρ started off at $1/\tau = 25$, marginally too large to allow salt-sheet instability, and then decreased slightly to 23. This decrease renders

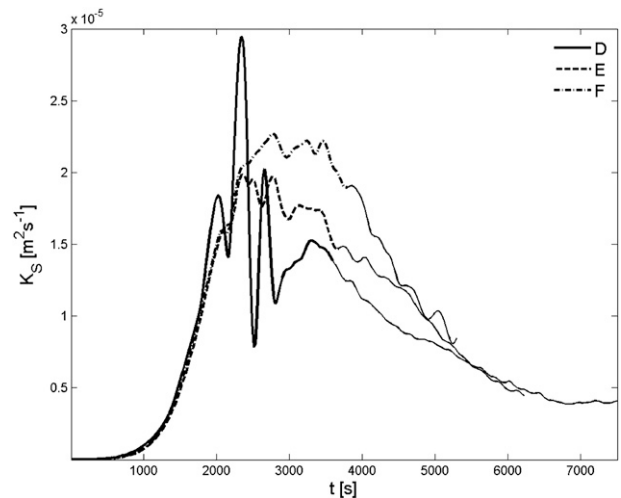


FIG. 13. (a) Evolution of the saline diffusivity for $R_\rho = 1.6$ and $Ri = 0.18$ (case D), 0.25 (case E), and 0.5 (case F).

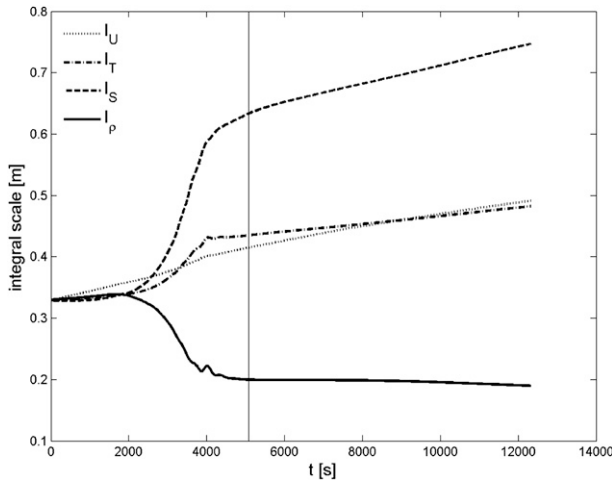


FIG. 14. Evolution of the integral scales for velocity (dotted), thermal buoyancy (dashed-dotted), saline buoyancy (dashed), and net buoyancy (solid) for case C. The vertical line is the point where disturbances first reach the upper or lower boundary.

salt-sheet mode marginally unstable, though no such instability is evident.

These results are consistent with our previous observation that salt sheets dominate in the cases with $R_\rho \leq 2$, whereas KH dominates when $R_\rho \geq 2$. This result pertains,

of course, to flows where $Ri = 0.18$ and the Reynolds number is not particularly large. The competition between the two instabilities could come out differently in other regions of parameter space.

In Fig. 16, we examine the influence of Ri by comparing case D ($R_\rho = 1.6$ and $Ri = 0.18$) with cases E and F, in which Ri is increased enough to remove the effect of KH instability and to greatly decrease the effect of shear on salt sheets in the nonlinear regime. Increasing Ri (or reducing shear) increases the thinning of the buoyancy layer by a few tens of percent. We conclude that shear, via a variety of effects including KH instability, impedes the thinning of the buoyancy layer by salt sheets.

The effect of shear on the evolution of the bulk Richardson number (Fig. 16b) is more pronounced. In case B, Ri starts off at its initial value 0.18 but quickly increases enough to exceed the KH extinction threshold 0.32 (Thorpe 1971; Smyth and Moum 2000b). The increase becomes most rapid with the onset of the propagating secondary instability (section 3). In case F, the rise in Ri is the most rapid of all. A similar result holds for the velocity-density scale ratio R , which starts off at unity in all cases but rises rapidly with secondary instability. The rise is most pronounced in the high Ri case. The likelihood of Holmboe instability developing depends on the

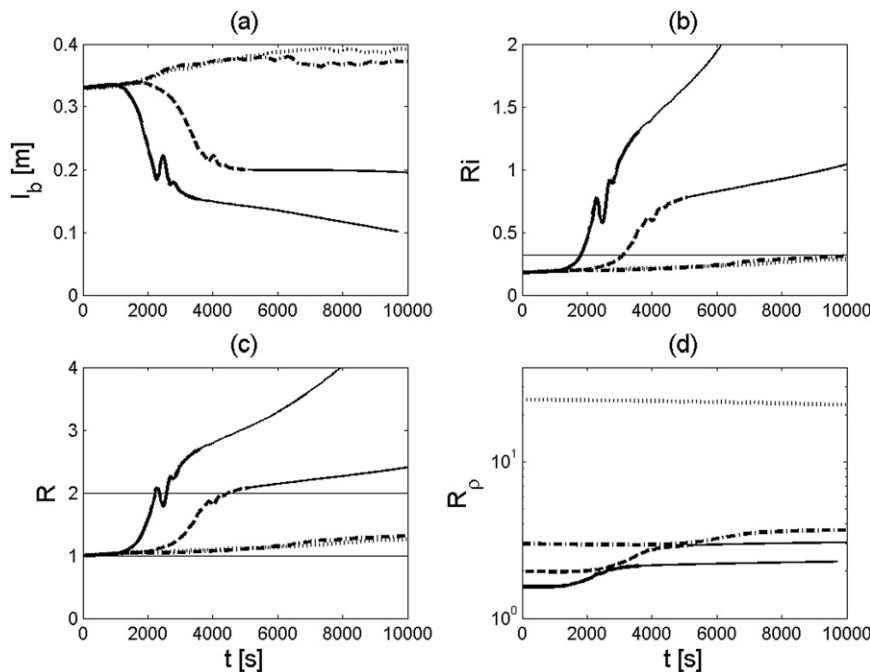


FIG. 15. (a) Evolution of the integral scale for four values of R_ρ . Dotted line is for $R_\rho = 25$ (case A); dashed-dotted line is for $R_\rho = 3$ (case B); dashed line is for $R_\rho = 2$ (case C); and solid line is for $R_\rho = 1.6$ (case D). In each case, the thick curve is terminated when buoyant fluid reaches the upper and lower boundaries. Evolution of (b) Ri , (c) R , and (d) R_ρ for the same cases. Horizontal lines show (b) the terminal value $Ri = 0.32$ and (c) the initial value $R = 1$ and the value $R = 2$ needed for Holmboe instability (Alexakis 2005).

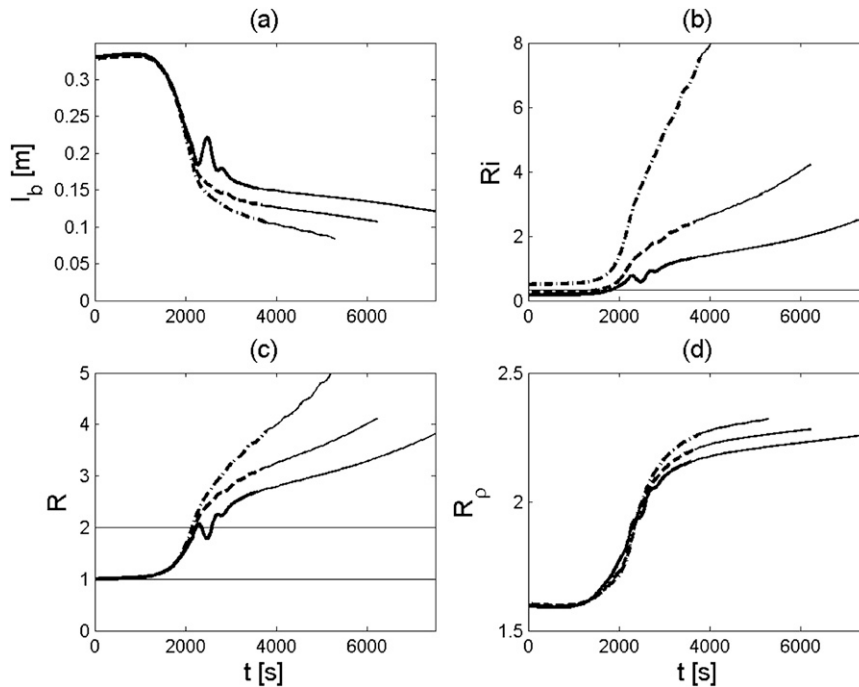


FIG. 16. (a) Evolution of the integral scale for three values of Ri. In each case, $R_p = 1.6$. Solid line is for $Ri = 0.18$ (case D); dashed line is for $Ri = 0.25$ (case E); and dashed–dotted line is for $Ri = 0.50$ (case F). In each case, the thick curve is terminated when buoyant fluid reaches the upper and lower boundaries. Evolution of (b) Ri, (c) R and (d) R_p for the same cases.

combination of R and Ri : increasing R increases the Holmboe growth rate, and increasing Ri decreases the growth rate [at least beyond about $Ri \sim O(1)$] but never extinguishes it entirely.

Finally, the effect of initial Ri on the evolution of R_p is slight. In each case, R_p increases rapidly to ~ 2.3 with secondary instability onset and then more slowly after that. Hence, the layer’s ability to support double diffusion is reduced somewhat. This tendency is greatest when Ri is large (Fig. 16d, dashed–dotted).

6. The dissipation ratio

The dissipation ratio Γ (Oakey 1985) is useful for distinguishing mixing due to salt fingering from that due to shear-driven turbulence (e.g., McDougall and Ruddick 1992; St. Laurent and Schmitt 1999; Inoue et al. 2008),

$$\Gamma = \frac{\chi_T \langle B_z \rangle}{2 \epsilon \langle B_{Tz}^2 \rangle}. \tag{22}$$

Here,

$$\chi_T = 2k_T \left\langle \left(\frac{\partial b'_T}{\partial x_i} \right)^2 \right\rangle \text{ and} \tag{23}$$

$$\epsilon = \frac{\nu}{2} \left\langle \left(\frac{\partial u'_i}{\partial x_j} + \frac{\partial u'_j}{\partial x_i} \right)^2 \right\rangle \tag{24}$$

are the dissipation rates for thermal buoyancy variance and perturbation kinetic energy, respectively. Angle brackets represent a volume average over a thin layer surrounding the center of the interfacial layer, $-h/4 \leq z \leq h/4$. It is typically found that $\Gamma \approx 0.2$ for shear-driven turbulence, whereas $\Gamma \geq 0.5$ for salt fingering (e.g., Hamilton et al. 1989; St. Laurent and Schmitt 1999; Smyth and Kimura 2007).

This expectation is confirmed in the present DNS results. Figure 17a shows $\Gamma(t)$ for a sequence of cases with $Ri = 0.18$ and $R_p = 1.6$ (solid), 2 (dashed), 3 (dashed–dotted), and 25 (dotted). In each case, during the initial instability and transition to turbulence, Γ was highly variable and generally > 0.2 but approached a quasi-steady state in the later stages.

In case A (dotted), R_p was too large to allow salt sheets to grow and the mixing was purely shear driven. The equilibrium value has Γ very close to 0.2 (cf. Smyth et al. 2001). In the contrasting case D (solid), R_p was much smaller and salt-sheet mixing was dominant. In that case, Γ remains large and approaches an equilibrium value > 0.5 .

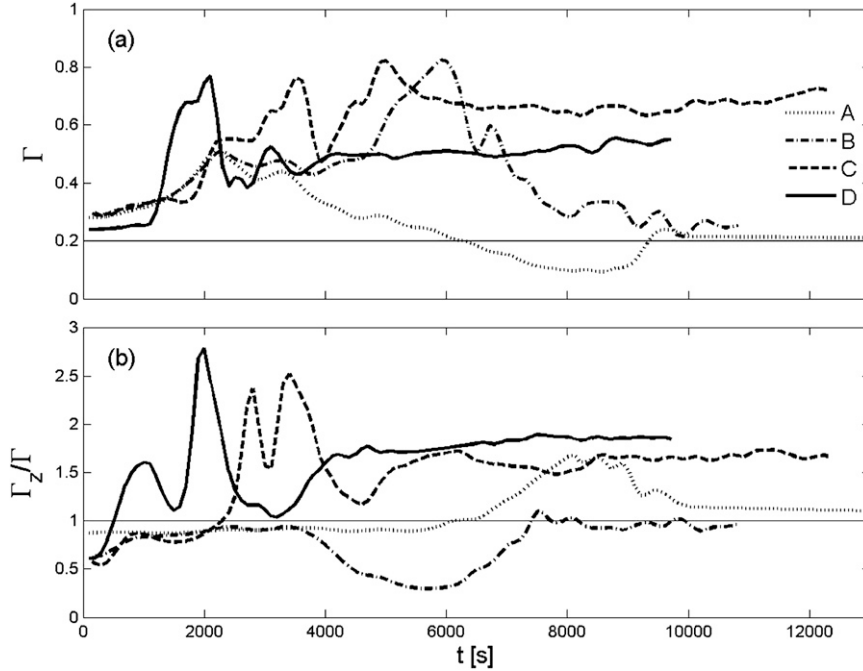


FIG. 17. (a) Evolution of the dissipation ratio Γ for $Ri = 0.18$ and $R_p = 25$ (case A), 3 (case B), 2 (case C), and 1.6 (case D). The horizontal line shows $\Gamma = 0.2$. (b) The ratio Γ_z/Γ for the same four cases. The horizontal line shows unity.

In the intermediate case C (dashed), $R_p = 2$ and the linear growth rates of KH and salt-sheet instabilities are equal, but we have seen previously that salt sheets dominate the mixing statistics. Consistently with this, Γ approaches a large value characteristic of salt fingering. The second intermediate case B (dashed-dotted), with $R_p = 3$, was dominated by KH instability, although salt fingering was present. In this case, Γ remains large until relatively late in the simulation ($t \sim 7000$ s) but eventually drops to a value near 0.2 consistent with shear-driven mixing.

Observational estimates of Γ are often made using vertical profiles, so χ_T and ϵ are approximated by their isotropic equivalents,

$$\chi_{Tz} = 6\kappa_T \left\langle \left(\frac{\partial b'_T}{\partial z} \right)^2 \right\rangle \quad \text{and} \quad (25)$$

$$\epsilon_z = \frac{15}{4} \nu \left\langle \left(\frac{\partial u}{\partial z} \right)^2 + \left(\frac{\partial v}{\partial z} \right)^2 \right\rangle \quad (26)$$

(which become exact when the dissipation scales are isotropic). In shear-driven turbulence, gradients can be dominated by the vertical derivative, in which case both χ_T and ϵ can be significantly overestimated (Itsweire et al. 1993; Smyth and Moum 2000a). In laminar salt fingering, horizontal gradients dominate, so the reverse result is to be expected. In either case, it is reasonable to hope that

much of the discrepancy will cancel out when the ratio of χ_{Tz} and ϵ_z is taken in (22) to obtain the approximation Γ_z . This appears to be true in the shear-dominated cases A and B (Fig. 17b). Instantaneous values fluctuate significantly, but in the eventual equilibrium state Γ is well approximated by Γ_z . In contrast, Γ_z overestimates Γ by 50%–100% in the salt-sheet-dominated cases C and D. Similar results have been found by Kimura et al. (2011) in DNS of weakly sheared layers.

To see the effect of varying Ri , case D, with $R_p = 1.6$ and $Ri = 0.18$, was repeated at two values of Ri large enough to eliminate KH instability, 0.25 and 0.50 (Fig. 18). Again, there was considerable fluctuation in the initial stages, with both Γ and Γ_z generally being larger in the higher Ri cases. As the flows settled down to the quasi-equilibrium state, however, all three converged to the same result, with Γ near 0.5 (Fig. 18a) and Γ_z about twice that (Fig. 18b). As with previous mixing statistics (section 4b), the presence of KH instability in the case with $Ri = 0.18$ makes virtually no difference; Γ and Γ_z remain characteristic of salt fingering.

7. Dependence on diffusivity and aspect ratios

The diffusivity ratio τ and the aspect ratio μ together determine the memory needed for DNS. The smallest scale that must be resolved is the saline Batchelor scale,

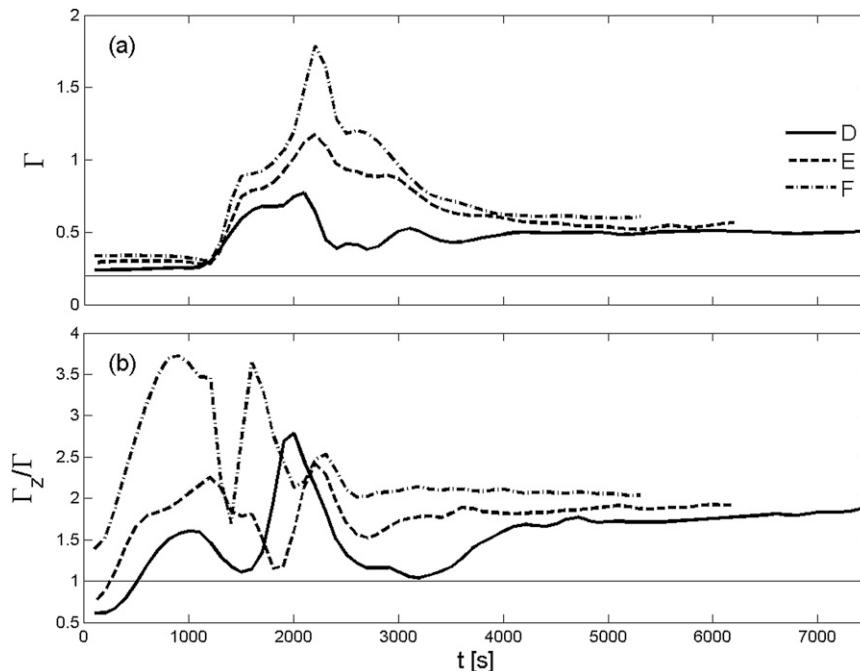


FIG. 18. (a) Evolution of the dissipation ratio Γ for $R_\rho = 1.6$ and $Ri = 0.18$ (case D), 0.25 (case E), and 0.50 (case F). The horizontal line shows $\Gamma = 0.2$. (b) The ratio Γ_z/Γ for the same cases. The horizontal line shows unity.

proportional to $\tau^{1/2}$, whereas the layer thickness, and hence the domain size, is proportional to μ^{-1} . In the present study, τ exceeds the value for saltwater by a factor of 4; hence, $\tau^{1/2}$ is too large by a factor of 2. The aspect ratio corresponds to an interfacial layer with thickness on the order of 1 m, whereas a typical oceanic value is 2–5 m (Kunze 2003). In more general flow geometries, breaking internal waves could generate shear layers even thicker than this. To attain true oceanic values will therefore require at least $(2 \times 2)^3 = 64$ times the memory used here, a requirement that is not far from being met as this is written. Here, we describe a brief sequence of experiments designed to provide a glimpse of the results when τ and μ take more realistic values.

The effect of τ is straightforward: reducing its value enhances double-diffusive mixing processes. Figure 19 shows the saline diffusivity for two cases. In the first (dashed curve), $\tau = 0.01$, the value for seawater. In the second (solid), τ is artificially increased to 0.04 as has been done for all other cases considered here. To save processing time, the domain width L_y was reduced to $2\lambda_S$ for both of these runs. (The difference due to this change is minor, as we have confirmed via comparison of cases Ct04 and C.) The maximum diffusivity is higher by a factor of 2–3 when $\tau = 0.01$; that is, the artifice of increasing τ tends to weaken the salt-sheet instability that drives the salt flux.

This result is in accord with the previous DNS of Kimura and Smyth (2007).

The dependence on μ is less obvious. Recall that μ is the ratio of salt-sheet wavelength to layer thickness, and it is proportional to $Re^{-1/2} Ri^{-1/4}$. When μ is decreased (with Ri fixed), the central region is dominated by a persistent KH billow (Fig. 20). Salt sheets are relegated to the relatively weak double-diffusive gradients remaining at the outer edges of the layer.

The tendency for KH modes to dominate with decreasing μ is also evident in the saline diffusivity (Fig. 21). Early in the evolution, K_S is relatively large in the low μ case because of the large KH instability (dashed-dotted curve, $1000 \text{ s} < t < 2000 \text{ s}$). Later, however, there is no sign of the increased diffusivity because of the propagating mode, as is evident in case C and even more so in case Cm13 (with increased μ). This is consistent with the result shown in Fig. 20 and indicates that, in a thicker interface, enhanced KH instability tends to mix out salt sheets and their resulting propagating modes, thereby leading to reduced diffusivity.

Although we do not show it here, reduced μ also reduces the tendency for the stratified layer to become thinner and likewise the increase in the scale ratio R . These tendencies are opposite when τ is reduced to 0.01, because that change reinforces salt sheets.

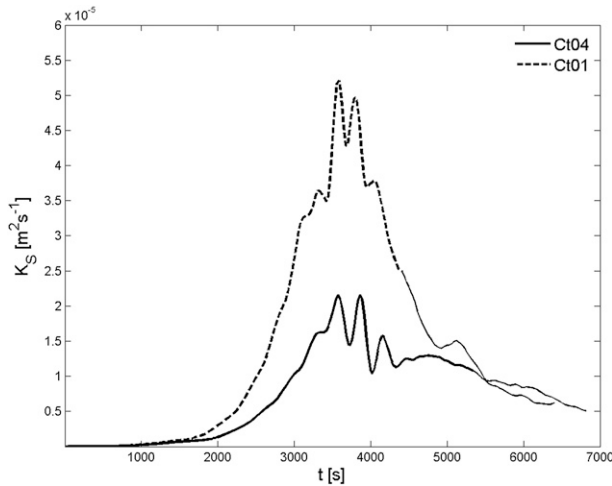


FIG. 19. Evolution of the saline diffusivity for $\tau = 0.04$ (case Ct04) and 0.01 (case Ct01).

8. Conclusions

Our goal has been to capture the effect of shear on salt fingering over a realistic range of R_ρ , with Ri small enough to allow KH instability. Periodicity intervals in the horizontal directions have been chosen just large enough to accommodate the largest-scale instabilities based on previous theoretical work. Economy has been essential in these choices, because the spatial resolution requirement for salinity, even with τ increased to 0.04, is severe.

The case we have focused most on had initial layer half thickness $h = 0.16$ m. This half-layer thickness is smaller than observations [in staircases, $O(1$ m) is typical; e.g., Kunze 2003], but it quickly expands (Fig. 14). At $t = 0$, we assume that the interface has a simple hyperbolic tangent form, with temperature, salinity, and horizontal velocity all changing over the same vertical distance. There is no particular reason to assume that these length scales are all the same. Observations (Gregg and Sanford 1987) do not rule out a factor of 2 difference, which could lead to a different class of shear instabilities (Holmboe instead of KH). Nonetheless, the assumption of equal scales is the simplest place to begin. Given enough time, the flow might evolve to a stationary state with realistic mean profiles, but vertically propagating disturbances eventually reach the upper and lower boundaries and the resulting unphysical effects propagate into the interfacial layer not long afterward, limiting the duration over which results are meaningful.

In summary, we simulate a relatively thin interface evolving over a limited time from an initial condition that may never actually be realized in the ocean. Despite these limitations, our DNS have revealed a rich interplay between shear and double-diffusive effects that we believe provides insight applicable to observed thermohaline

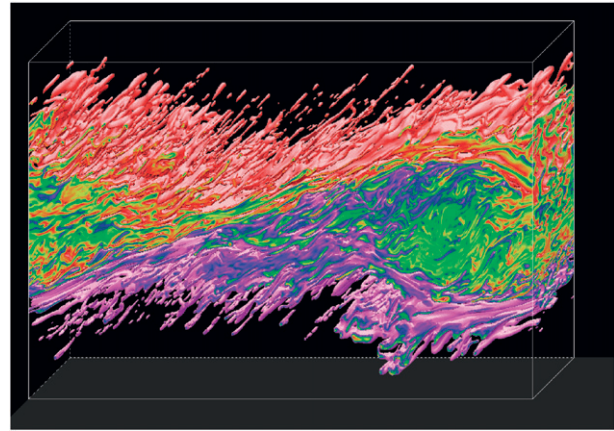


FIG. 20. Salinity field for $\mu = 0.064$ (case Cm06) at $t = 3700$ s. The vertical range shown is $-3/16L_z \leq z \leq 3/16L_z$. Colors range from $-0.6\Delta B_S$ (purple) to $0.6\Delta B_S$ (red); values outside this range are rendered transparent.

staircases and other salt-fingering regimes in the thermocline. They also form a foundation for future studies where the ongoing growth of computational hardware will allow more realistic parameter choices.

Subject to the foregoing caveats, we offer the following conclusions:

- 1) In a vertically localized layer with stratification unstable to salt fingering ($1 < R_\rho < 1/\tau$) and moderate shear ($Ri < 1/4$, but not by much), both salt-sheet and KH instability mechanisms operate. Either can dominate, depending mainly on the values of Ri and R_ρ . Each mechanism has one or more characteristic secondary instabilities (zigzag and tip modes for SS and KP mode for KH), and these various modes can combine at finite amplitude to create new flow features.
- 2) A new secondary instability is driven by the combination of KH billows and salt sheets: buoyant fluid near the tips of salt sheets develops a highly localized propagating instability due to the straining of currents surrounding the KH billows. This can excite streamwise dependence on a wide range of scales, leading to both oscillatory features on the scale of the billow and small-scale plumes related to the tip mode.
- 3) After the transition to turbulence, mixing statistics may be dominated by either the KH or the SS mechanism. In the former case, the turbulence has downward buoyancy flux characteristic of shear forcing; in the latter, the buoyancy flux is upward because of convective forcing. The case where the linear growth rates of KH and SS are equal is dominated by SS, because Ri grows more rapidly than R_ρ .

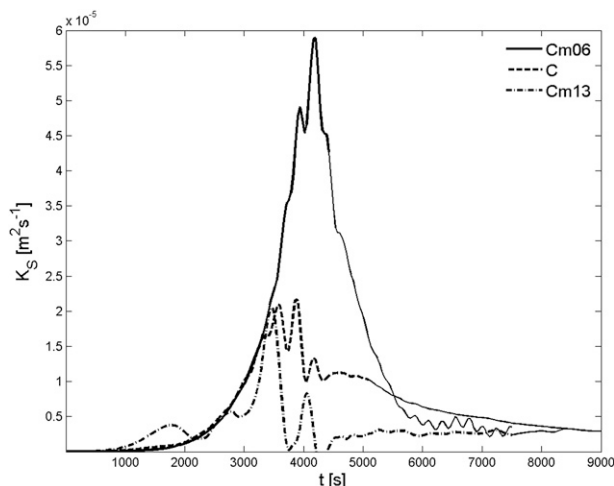


FIG. 21. (a) Evolution of the saline diffusivity for $\mu = 0.13$ (case Cm13), 0.10 (case C), and 0.064 (case Cm06).

- 4) Fluxes across the interface are reasonably well described by laboratory-based “thin layer” laws. This, in combination with the fact that the duration of the event scales well with the e -folding time of the primary instability, allows parameterization of the net (time integrated) buoyancy flux across the interface.
- 5) Turbulent diffusivities decrease monotonically with increasing shear, despite the additional source of kinetic energy for mixing that shear represents. This has significant implications for the design of subgrid models used to model a wide range of phenomena, from finescale interleaving (e.g., Smyth and Ruddick 2010) to basin-scale circulations (e.g., Large et al. 1994).
- 6) For the case with equal linear growth rates, the flux ratio γ exhibits combined effects of shear and double-diffusive forcing early in the flow evolution. After the flow becomes turbulent, γ asymptotes to a value remarkably close to the prediction of linear theory for the fastest-growing salt-sheet mode.
- 7) Like γ , the Schmidt number (ratio of effective viscosity to effective saline diffusivity) shows early influences of KH and salt-sheet instabilities and then returns to a near-linear value in the turbulent regime. The smallness of these values [$Sc \sim O(10^{-1})$ or less] confirms earlier predictions that salt sheets are “slippery”; that is, they are poor conductors of momentum. We note that this result pertains to the case of a steady background shear; an evolving shear might be impacted differently. Of particular relevance is the case of inertially rotating shear (e.g., Kunze 1990). In this case, instability evolution is likely to be sensitive to the periodic boundary conditions and may require a significantly larger horizontal domain as a result. This case is deferred to a future study.

- 8) As the salinity and temperature profiles thicken because of mixing, the density profile thins. This is consistent with the explanation for the maintenance of thermohaline staircases by Schmitt (1994). Mixing also leads to changes in the bulk Richardson number, the velocity–density scale ratio, and the density ratio that explain how the KH and salt-sheet mechanisms evolve over time. The increase in the scale ratio (largely due to the thinning of the buoyancy profile) emphasizes the potential importance of Holmboe-like (oscillatory) instability (e.g., Holmboe 1962; Alexakis 2005; Smyth et al. 2007) in thermohaline staircases.
- 9) The dissipation ratio Γ asymptotes to a value close to 0.2 when shear forcing is dominant. When salt sheets dominate, $\Gamma > 0.5$. This supports the use of Γ as a diagnostic to identify observed mixing events (e.g., St. Laurent and Schmitt 1999; Inoue et al. 2008).
- 10) When mixing is dominated by salt sheets, the isotropic approximation used in interpreting profiler data gives Γ too large by a factor of 1.5–2. This unexpected result (see also Kimura et al. 2011) suggests that the interpretation of oceanic measurements using Γ_z may need to be revisited.

As computational resources expand to allow more realistic simulations, the competition between shear and double-diffusive mixing will be altered. Reduction of τ to its oceanic value will favor salt sheets; increased layer thickness will favor shear instability. Which mixing process will dominate for given values of Ri and R_ρ remains to be seen, but present results suggest that salt-sheet effects will overwhelm shear forcing for $Ri \sim 0.18$ or greater and for $R_\rho \sim 2$ or less. The ultimate effect of these changes on mixing also remains to be determined.

Acknowledgments. This paper was much improved thanks to constructive comments by Timour Radko, two anonymous reviewers, and the editor. This research was funded by the National Science Foundation under Grant OCE-0453140. Computations were done using the supercomputing facilities at the National Center for Atmospheric Research in Boulder, Colorado. Rita Brown provided editorial assistance.

REFERENCES

- Alexakis, A., 2005: On Holmboe’s instability for smooth shear and density profiles. *Phys. Fluids*, **17**, 84–103.
- Collins, D., and S. Maslowe, 1988: Vortex pairing and resonant wave interactions in a stratified free shear layer. *J. Fluid Mech.*, **191**, 465–480.
- De Silva, I. P. D., H. J. S. Fernando, F. Eaton, and D. Hebert, 1996: Evolution of Kelvin-Helmholtz billows in nature and laboratory. *Earth Planet. Sci. Lett.*, **143**, 217–231.
- Fernandes, A., and R. Krishnamurti, 2010: Salt finger fluxes in a laminar shear flow. *J. Fluid Mech.*, **658**, 148–165.

- Geyer, W., and J. Smith, 1987: Shear instability in a highly stratified estuary. *J. Phys. Oceanogr.*, **17**, 1668–1679.
- , A. Lavery, M. Scully, and J. Trowbridge, 2010: Mixing by shear instability at high Reynolds number. *Geophys. Res. Lett.*, **37**, L22607, doi:10.1029/2010GL045272.
- Gregg, M. C., 1987: Diapycnal mixing in the thermocline: A review. *J. Geophys. Res.*, **92** (C5), 5249–5286.
- , 1998: Estimation and geography of diapycnal mixing in the stratified ocean. *Physical Processes in Lakes and Oceans*, J. Imberger, Ed., Coastal and Estuarine Studies, Vol. 54, Amer. Geophys. Union, 305–338.
- , and T. Sanford, 1987: Shear and turbulence in thermohaline staircases. *Deep-Sea Res.*, **34**, 1689–1696.
- Hamilton, J., M. Lewis, and B. Ruddick, 1989: Vertical fluxes of nitrate associated with salt fingers in the world's oceans. *J. Geophys. Res.*, **94**, 2137–2145.
- Hazel, P., 1972: Numerical studies of the stability of inviscid parallel shear flows. *J. Fluid Mech.*, **51**, 39–62.
- Hebert, D., 1988: Estimates of salt-finger fluxes. *Deep-Sea Res.*, **35**, 1887–1901.
- Holmboe, J., 1962: On the behaviour of symmetric waves in stratified shear layers. *Geophys. Publ.*, **24**, 67–113.
- Holyer, J., 1984: The stability of long, steady, two-dimensional salt fingers. *J. Fluid Mech.*, **147**, 169–185.
- Howard, L., 1961: Note on a paper of John W. Miles. *J. Fluid Mech.*, **10**, 509–512.
- Inoue, R., E. Kunze, L. St. Laurent, R. W. Schmitt, and J. M. Toole, 2008: Evaluating salt-fingering theories. *J. Mar. Res.*, **66**, 413–440.
- Itswire, E., J. Koseff, D. Briggs, and J. Ferziger, 1993: Turbulence in stratified shear flows: Implications for interpreting shear-induced mixing in the ocean. *J. Phys. Oceanogr.*, **23**, 1508–1522.
- Kelley, D., 1986: Oceanic thermohaline staircases. Ph.D. thesis, Dalhousie University, 333 pp.
- Kimura, S., and W. Smyth, 2007: Direct numerical simulations of salt sheets and turbulence in a double-diffusive shear layer. *Geophys. Res. Lett.*, **34**, L21610, doi:10.1029/2007GL031935.
- , —, and E. Kunze, 2011: Turbulence in a sheared, salt-fingering-favorable environment: Anisotropy and effective diffusivities. *J. Phys. Oceanogr.*, **41**, 1144–1159.
- Klaassen, G., and W. Peltier, 1985: The evolution of finite-amplitude Kelvin-Helmholtz billows in two spatial dimensions. *J. Atmos. Sci.*, **42**, 1321–1339.
- , and —, 1989: The role of transverse secondary instabilities in the evolution of free shear layers. *J. Fluid Mech.*, **202**, 367–402.
- , and —, 1991: The influence of stratification on secondary instability in free shear layers. *J. Fluid Mech.*, **227**, 71–106.
- Kunze, E., 1987: Limits on growing, finite-length salt fingers: A Richardson number constraint. *J. Mar. Res.*, **45**, 533–556.
- , 1990: The evolution of salt fingers in inertial wave shear. *J. Mar. Res.*, **48**, 471–504.
- , 1994: A proposed flux constraint for salt fingers in shear. *J. Mar. Res.*, **52**, 999–1016.
- , 2003: A review of oceanic salt fingering theory. *Prog. Oceanogr.*, **56**, 399–417.
- , A. Williams, and R. Schmitt, 1987: Optical microstructure in the thermohaline staircase east of Barbados. *Deep-Sea Res.*, **34**, 1697–1704.
- Large, W., J. McWilliams, and S. Doney, 1994: Ocean vertical mixing: A review and a model with a nonlocal boundary layer parameterization. *Rev. Geophys.*, **32**, 363–403.
- Linden, P., 1974: Salt fingers in a steady shear flow. *Geophys. Fluid Dyn.*, **6**, 1–27.
- McDougall, T., and J. Taylor, 1984: Flux measurements across a finger interface at low values of the stability ratio. *J. Mar. Res.*, **42**, 1–14.
- , and B. Ruddick, 1992: The use of ocean microstructure to quantify both turbulent mixing and salt fingering. *Deep-Sea Res.*, **39**, 1931–1952.
- Miles, J., 1961: On the stability of heterogeneous shear flows. *J. Fluid Mech.*, **10**, 496–508.
- Mueller, R. D., W. D. Smyth, and B. R. Ruddick, 2007: Shear and convective turbulence in a model of thermohaline intrusions. *J. Phys. Oceanogr.*, **37**, 2534–2549.
- Muller, P., G. Holloway, F. Henyey, and N. Pomphrey, 1986: Nonlinear interactions among internal gravity waves. *Rev. Geophys.*, **24**, 493–536.
- Munk, W., and C. Wunsch, 1998: Abyssal recipes II: Energetics of tidal and wind mixing. *Deep-Sea Res.*, **45**, 1977–2010.
- Oakey, N., 1985: Statistics of mixing parameters in the upper ocean during JASIN phase 2. *J. Phys. Oceanogr.*, **15**, 1662–1675.
- Radko, T., and M. Stern, 2011: Finescale instabilities of the double-diffusive shear flow. *J. Phys. Oceanogr.*, **41**, 571–585.
- Ruddick, B., and O. Kerr, 2003: Oceanic thermohaline intrusions: Theory. *Prog. Oceanogr.*, **56**, 483–497.
- , and K. Richards, 2003: Oceanic thermohaline intrusions: Observations. *Prog. Oceanogr.*, **56**, 499–527.
- , T. McDougall, and J. Turner, 1989: The formation of layers in a uniformly stirred density gradient. *Deep-Sea Res.*, **36**, 579–609.
- Schmitt, R. W., 1979a: Flux measurements on salt fingers at an interface. *J. Mar. Res.*, **37**, 419–436.
- , 1979b: The growth rate of super-critical salt fingers. *Deep-Sea Res.*, **26A**, 23–44.
- , 1994: Triangular and asymmetric salt fingers. *J. Phys. Oceanogr.*, **24**, 855–860.
- , 2003: Observational and laboratory insights into salt finger convection. *Prog. Oceanogr.*, **56**, 419–433.
- , H. Perkins, J. Boyd, and M. Stalcup, 1987: C-SALT: An investigation of the thermohaline staircase in the western tropical North Atlantic. *Deep-Sea Res.*, **34**, 1655–1665.
- , J. Ledwell, E. Montgomery, K. Polzin, and J. Toole, 2005: Enhanced diapycnal mixing by salt fingers in the thermocline of the tropical Atlantic. *Science*, **308**, 685–688.
- Seim, H., and M. Gregg, 1994: Detailed observations of a naturally-occurring shear instability. *J. Geophys. Res.*, **99** (C5), 10 049–10 073.
- Smyth, W. D., 2003: Secondary Kelvin-Helmholtz instability in a weakly stratified shear flow. *J. Fluid Mech.*, **497**, 67–98.
- , and J. N. Moum, 2000a: Anisotropy of turbulence in stably stratified mixing layers. *Phys. Fluids*, **12**, 1343–1362.
- , and —, 2000b: Length scales of turbulence in stably stratified mixing layers. *Phys. Fluids*, **12**, 1327–1342.
- , and S. Kimura, 2007: Instability and diapycnal momentum transport in a double-diffusive, stratified shear layer. *J. Phys. Oceanogr.*, **37**, 1551–1565.
- , and B. R. Ruddick, 2010: Effects of ambient turbulence on interleaving at a baroclinic front. *J. Phys. Oceanogr.*, **40**, 685–712.
- , J. N. Moum, and D. R. Caldwell, 2001: The efficiency of mixing in turbulent patches: Inferences from direct simulations and microstructure observations. *J. Phys. Oceanogr.*, **31**, 1969–1992.
- , J. D. Nash, and J. N. Moum, 2005: Differential diffusion in breaking Kelvin-Helmholtz billows. *J. Phys. Oceanogr.*, **35**, 1004–1022.

- , J. R. Carpenter, and G. A. Lawrence, 2007: Mixing in symmetric Holmboe waves. *J. Phys. Oceanogr.*, **37**, 1566–1583.
- Stern, M., 1960: The salt fountain and thermohaline convection. *Tellus*, **12**, 172–175.
- , 1967: Lateral mixing of water masses. *Deep-Sea Res.*, **14**, 747–753.
- , 1969: Collective instability of salt fingers. *J. Fluid Mech.*, **35**, 209–218.
- , 1975: *Ocean Circulation Physics*. Academic Press, 246 pp.
- , and J. Simeonov, 2005: The secondary instability of salt fingers. *J. Fluid Mech.*, **533**, 361–380.
- , T. Radko, and J. Simeonov, 2001: Salt fingers in an unbounded thermocline. *J. Mar. Res.*, **59**, 355–390.
- St. Laurent, L., and R. Schmitt, 1999: The contribution of salt fingers to vertical mixing in the North Atlantic Tracer Release Experiment. *J. Phys. Oceanogr.*, **29**, 1404–1424.
- Thorpe, S., 1971: Experiments on the instability of stratified shear flows: Miscible fluids. *J. Fluid Mech.*, **46**, 299–319.
- , 1987: Transition phenomena and the development of turbulence in stratified fluids. *J. Geophys. Res.*, **92**, 5231–5245.
- Walsh, D., and B. Ruddick, 1998: Nonlinear equilibration of thermohaline intrusions. *J. Phys. Oceanogr.*, **28**, 1043–1069.
- Wells, M., R. Griffiths, and J. Turner, 2001: Generation of density fine structure by salt fingers in a spatially periodic shear. *J. Geophys. Res.*, **106**, 7027–7036.
- Winters, K., J. MacKinnon, and B. Mills, 2004: A spectral model for process studies of rotating, density-stratified flows. *J. Atmos. Oceanic Technol.*, **21**, 69–94.
- Woods, J., 1968: Wave-induced shear instability in the summer thermocline. *J. Fluid Mech.*, **32**, 791–800.
- You, Y., 2002: A global ocean climatological atlas of the Turner angle: Implications for double diffusion and water-mass structure. *Deep-Sea Res.*, **49**, 2075–2093.